Informes Técnicos Ciemat

1284

Abril, 2013

Electron Cyclotron Waves Polarization in the TJ II Stellarator

Á. Cappa
J. Martínez-Fernández
D. Wagner

GOBIERNO DE ESPAÑA

MINISTERIO DE ECONOMÍA Y COMPETITIVIDAD

Ciemat
Centro de Investigaciones Energéticas, Medioambientales y Tecnológicas

Informes Técnicos Ciemat 1284
Abril, 2013

Electron Cyclotron Waves Polarization in the TJII Stellarator

Á. Cappa
J. Martínez-Fernández
D. Wagner

Laboratorio Nacional de Fusión por Confinamiento Magnético

Toda correspondencia en relación con este trabajo debe dirigirse al Servicio de Información y Documentación, Centro de Investigaciones Energéticas, Medioambientales y Tecnológicas, Ciudad Universitaria, 28040-MADRID, ESPAÑA.

Las solicitudes de ejemplares deben dirigirse a este mismo Servicio.

Los descriptores se han seleccionado del Thesauro del DOE para describir las materias que contiene este informe con vistas a su recuperación. La catalogación se ha hecho utilizando el documento DOE/TIC-4602 (Rev. 1) Descriptive Cataloguing On-Line, y la clasificación de acuerdo con el documento DOE/TIC.4584-R7 Subject Categories and Scope publicados por el Office of Scientific and Technical Information del Departamento de Energía de los Estados Unidos.

Catálogo general de publicaciones oficiales
http://www.060.es

Depósito Legal: M -26385-2011
ISSN: 1135 - 9420
NIPO: 721-13-023-X

Editorial CIEMAT

CLASIFICACIÓN DOE Y DESCRIPTORES

S70
POLARIZATION; WAVE PROPAGATION; THEORETICAL DATA; CALCULATION METHODS; STELLARATORS; PLASMA WAVES

Electron Cyclotron Waves Polarization in the TJII Stellarator

Cappa, Á.; Martínez-Fernández, J.; Wagner, D.

40 pp. 29 g. 13 ref.

Abstract:

This report describes the theoretical calculations related with the electron cyclotron (EC) waves polarization control in the TJII stellarator. Two main aspects will be distinguished: the determination of the vacuum polarization that the wave must exhibit if a given propagation mode in a cold plasma is desired and the calculation of the behavior of the grooved polarizers and other transmission systems used to launch the vacuum wave with the required polarization.

Polarización de Ondas Electrónicas Ciclotrónicas en el Stellarator TJII

Cappa, Á.; Martínez-Fernández, J.; Wagner, D.

40 pp. 29 g. 13 ref.

Resumen:

Este informe describe los cálculos teóricos implicados en el control de polarización de ondas electrónicas ciclotrónicas (EC) en el stellarator TJII. Se distinguirán dos aspectos principales: la determinación de la polarización que la onda ha de exhibir en vacío si se desea un determinado modo de propagación en un plasma frío y el cálculo del comportamiento de los polarizadores ranurados y otros sistemas de transmisión utilizados para emitir la onda en vacío con la polarización requerida.

Contents

1 Introduction

In the TJ–II stellarator, plasmas are created and heated by two 53.2 GHz gyrotrons, each of them delivering up to 300 kW of power. This power is transmitted from the gyrotrons to the plasma by means of two quasi-optical transmission lines (QTL1 and QTL2) located at stellarator symmetric positions (ports A6 and B3, see figure 1) [1].

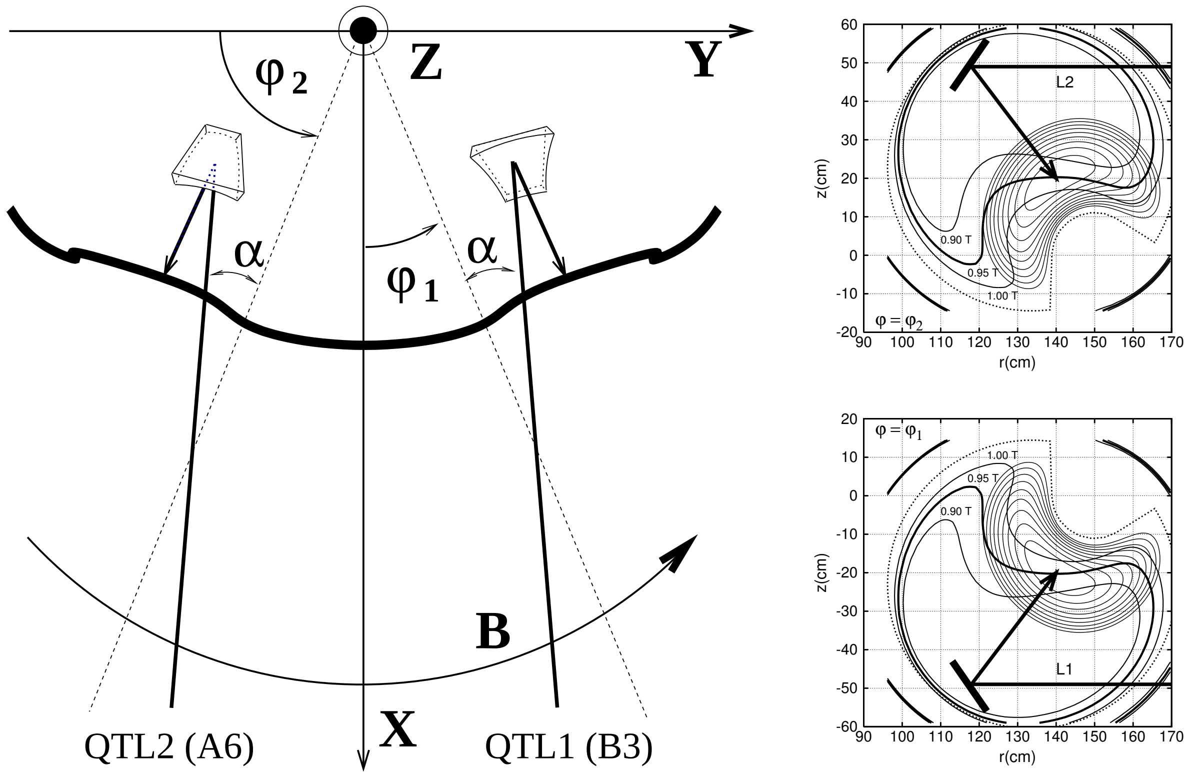

Figure 1: Launching configuration of the 53.2 GHz ECRH system. The magnetic axis (thick line) and the direction of the main magnetic field are shown on the left ($\alpha = 8.4°$, $\varphi_1 = 25.5°$ and $\varphi_2 = 64.5°$). On the right, the magnetic flux surfaces and the constant field contours are plotted for both launchers (L1 is located in the B sector of the device, at $\varphi = \varphi_1$, and L2 is located in the A sector at $\varphi = \varphi_2$). The beam path lies in a non toroidal plane and thus the trajectories plotted in the right panels are the projection of each beam path in the corresponding toroidal planes, given by φ_1 and φ_2. Vectors **X**, **Y**, and **Z** define the general TJ–II reference system. Note that the initial launching direction differs from the radial direction ($\alpha \neq 0$).

The launcher of each line is a steerable mirror which is located inside the vacuum vessel. Each of these internal mirrors allows us to launch the power at different locations along the magnetic axis and also to reach different off-axis positions independently (see figure 1) [2]. In addition, a 28 GHz ECRH heating system [3], designed for electron Bernstein waves excitation by the O–X–B mode conversion technique [4], and also equipped with an internal steerable mirror, is presently installed in the TJ–II D6 sector (see figure 2). For both systems, a complete control of the polarization of the launched waves is needed. In the case of the 53.2 GHz system (the main heating system), which can perform perpendicular and oblique injection with each launcher, good coupling of the quasi-extraordinary mode (QX) is desirable, particularly during ECCD on-axis experiments. Moreover, to reach an optimum Bernstein mode excitation, it is also mandatory to couple a pure QO–mode under oblique injection. Finally, an EBW emission diagnostic [5] is installed in the uppert part of the D6 sector and a knowledge of the theoretical polarization of the emitted wave at the detection antenna is needed for a proper interpretation of the results. To set-up the proper polarization, each transmission system is equipped with grooved mirror polarizers. In the case of QTL1 and the 28 GHz heating system, the polarization is controlled by a universal polarizer (two independent grooved mirrors with different corrugation depths) that allow us to convert the linear horizontal polarization produced by the gyrotrons into any desired elliptical polarization. The second transmission line is only equipped with one grooved mirror and therefore the available space of wave polarizations is restricted. Figures 3 and 4 show the setup of the polarizers in each case.

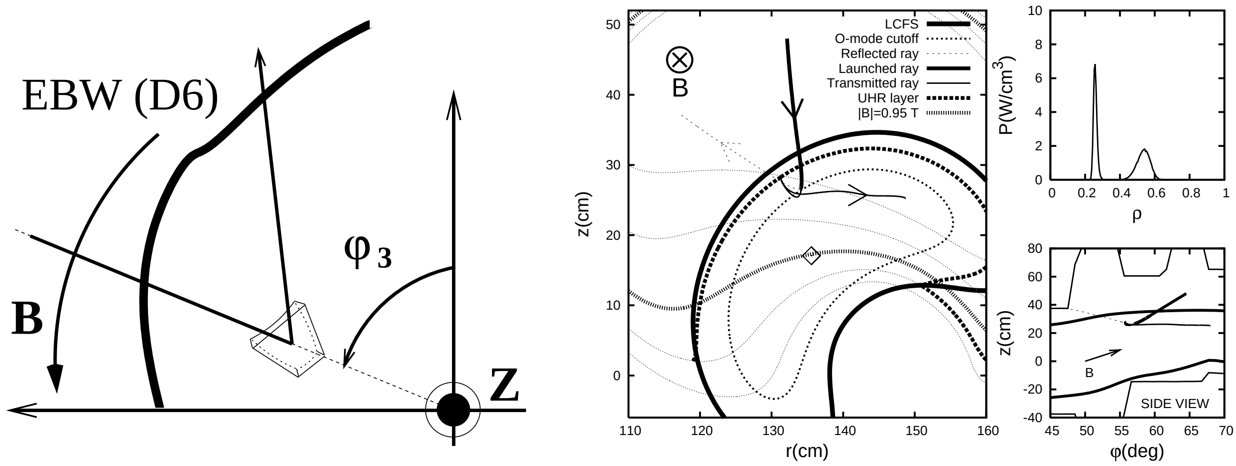

Figure 2: Launching configuration of the 28 GHz ECRH system. Since TJ–II has four periods, the A6 and D6 ports are equivalent ($\varphi_3 = \varphi_2$) and therefore the 53.2 GHz and the 28 GHz systems have similar launching configurations. Nevertheless, in this case, the EC power is initially injected along the radial direction. An EBW ray tracing calculation using the code TRUBA [6] is shown in the right viewgraph to illustrate the wave trajectory in the plasma. The projection of the launched, reflected and transmitted rays on the toroidal plane where O–X conversion occurs is shown, as well as the power deposition profile and a side view of the rays trajectories. The O-mode cutoff layer and the upper hybrid resonant layer are also shown.

The report is divided in three sections. In Section 2, a short review of the basic physics regarding wave polarization in cold plasmas is given. Section 3 presents a general calculation of the angles that define the desired polarization ellipse in a reference system suitable for the experiments. Next, in section 4, the theoretical analysis of the influence of grooved mirrors on wave polarization is presented. Moreover, the changes in the wave polarization induced by the bends of the 28 GHz waveguide are discussed. Then, the final dependence of the launched wave polarization on the rotation angles of the polarizers is given in the reference system introduced in the previous section. Appendix A summarizes the movement of the internal mirrors of the 53.2 GHz system and its relation with their positioning angles while appendix B presents the values of the polarization angles that are needed to couple a QX–mode in a wide range of launching directions. Finally, appendix C includes the dependence of the 28 GHz polarizers performance for different incidence angles.

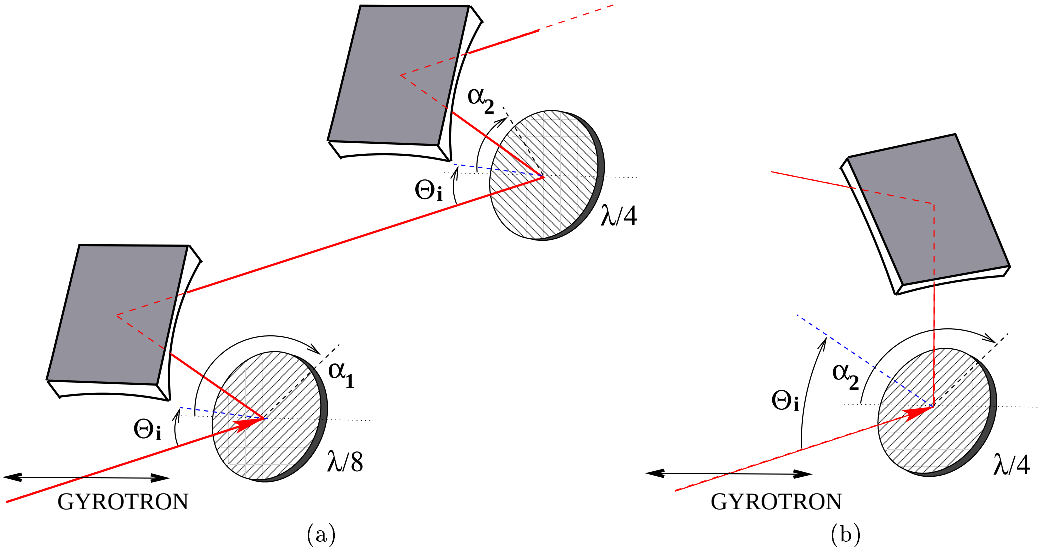

Figure 3: Grooved mirrors setup for QTL1 (left) and QTL2 (right). In the QTL1 case the incidence angle is $\Theta_i = 15°$ while in the QTL2 case we have $\Theta_i = 45°$.

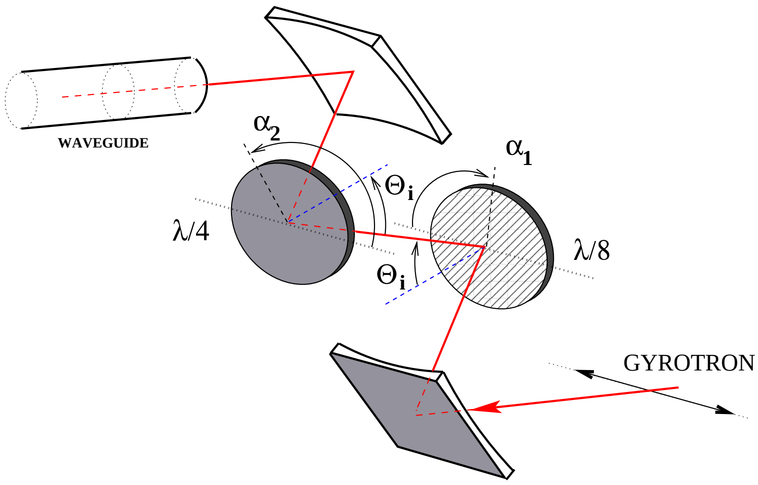

Figure 4: Grooved mirrors setup in the EBW heating system. Here, $\Theta_i = 30°$.

2 EC waves polarization in cold magnetized plasmas

In the Stix reference frame ($\mathbf{B}$ along z and $\mathbf{k}$ in the xz plane (see figure 5a), the components of the wave equation $\mathbf{N}\times\mathbf{N}\times\mathbf{E}+\bar{\bar{\epsilon}}\,\mathbf{E}=0$, for plane waves ($\mathbb{E}\equiv\mathbf{E}\,e^{i(\mathbf{k}\cdot\mathbf{r}-\omega t)}$) in a uniform cold magnetized electron plasma, are

$$\begin{aligned}&(S-N^2\cos^2\theta)E_x - iDE_y + N^2\cos\theta\sin\theta E_z = 0\\ &iDE_x + (S-N^2)E_y = 0\\ &N^2\cos\theta\sin\theta E_x + (P-N^2\sin^2\theta)E_z = 0\end{aligned} \tag{1}$$

where $\mathbf{N}\equiv\mathbf{k}c/\omega$. The quantities S, P and D are given by

$$\begin{aligned}S &= 1-\frac{{\omega_p}^2}{\omega^2-{\omega_c}^2}\\ D &= -\frac{\omega_c}{\omega}\left[\frac{{\omega_p}^2}{\omega^2-{\omega_c}^2}\right]\\ P &= 1-\frac{{\omega_p}^2}{\omega^2}\end{aligned} \tag{2}$$

and ω_p,ω_c,ω are the electron plasma frequency, the electron cyclotron frequency and the frequency of the considered wave respectively [7]. The angle θ is the wave propagation angle (angle between $\mathbf{k}$ and $\mathbf{B}$) and N^2 is the squared refraction index.

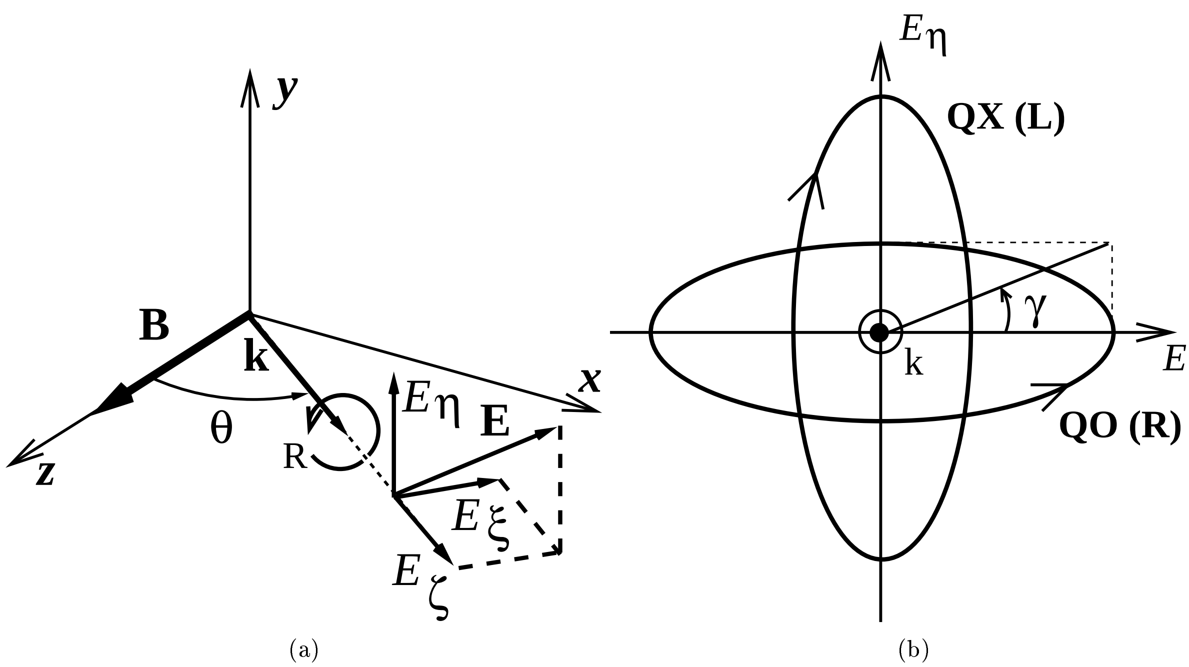

Figure 5: Stix frame (x,y,z) and wave reference system (ξ,η,ζ). The rotation sense of the right-handed (R) polarization ($iE_\xi/E_\eta>0$) in respect to $\mathbf{k}$ is shown on the left. Also, the QO–mode and QX–mode polarization ellipses in the wave reference system for oblique propagation with $\theta>\pi/2$ are represented on the right. In the case represented on the left, for which $\theta<\pi/2$, the QO–mode is left handed (L).

In vacuum, the electromagnetic field of a plane wave is transverse to the propagation direction $\mathbf{k}$. To investigate the coupling of the vacuum wave to the EC plasma wave it is convenient, in order to get an appropriate description of the EC wave polarization in the plasma, to define a new coordinates system — the wave reference system — that in this case is obtained from a rotation of angle θ in respect to the y direction (see figure 5a). The electric field components in the new frame are given by

$$\begin{pmatrix} E_\xi \\ E_\eta \\ E_\zeta \end{pmatrix} = \begin{pmatrix} \cos\theta & 0 & -\sin\theta \\ 0 & 1 & 0 \\ \sin\theta & 0 & \cos\theta \end{pmatrix} \begin{pmatrix} E_x \\ E_y \\ E_z \end{pmatrix} \tag{3}$$

Note that $E_\eta \equiv E_y$ and that E_ζ is the new longitudinal part of the field that develops in a magnetized plasma. Thus, using (1) together with the coordinates transformation, it is easily seen that

$$\frac{iE_\xi}{E_\eta} = \frac{iE_x}{E_y}\left[\cos\theta - \frac{E_z}{E_x}\sin\theta\right] = \frac{N^2 - S}{D}\left[\frac{P\cos\theta}{P - N^2\sin^2\theta}\right] \tag{4}$$

The left term of (4) is real and therefore the transverse polarization ellipses (projection of the general ellipses in the $\xi\eta$ plane) of both modes have their main axis directed along the ξ and the η directions respectively. The ratio iE_ξ/E_η defines the ellipticity angle where its sign defines the polarization rotation sense. Thus, in the wave system, we get four different cases

$$\begin{aligned} &\frac{iE_\xi}{E_\eta} = 0 && \rightarrow \text{Vertical linear polarization} \\ &\frac{iE_\xi}{E_\eta} = \infty && \rightarrow \text{Horizontal linear polarization} \\ &\frac{iE_\xi}{E_\eta} > 0 && \rightarrow \text{Right-handed polarization in respect to } \mathbf{k}(\text{R}) \\ &\frac{iE_\xi}{E_\eta} < 0 && \rightarrow \text{Left-handed polarization in respect to } \mathbf{k}(\text{L}) \end{aligned} \tag{5}$$

The solvability condition of (1) is of the type $AN^4 + BN^2 + C = 0$, which, for propagation with $N_x \neq 0$, leads to two electromagnetic solutions (the Appleton-Hartree solutions) usually referred as the *quasi ordinary* (QO) and the *quasi extraordinary* (QX) modes[1]. Introducing the refractive index of both electromagnetic solutions in (4) and taking the zero density limit ($\omega_p \to 0$) it can be demonstrated that

$$\boxed{\lim_{\omega_p \to 0} \frac{E_\xi}{E_\eta} = \frac{2\cos\theta}{ic(\sin^2\theta \pm \rho)} = \frac{ic(\sin^2\theta \mp \rho)}{2\cos\theta}} \tag{6}$$

where ρ is given by

$$\rho^2 = \sin^4\theta + \frac{4}{c^2}\cos^2\theta \tag{7}$$

and $c \equiv \omega_c/\omega$. The upper sign in both expressions appearing in (6) corresponds to the QX–mode while the lower one refers to the QO–mode. Using (6) it can be shown that both modes are orthogonal ($\mathbf{E}_{\text{QX}} \cdot \mathbf{E}_{\text{QO}}{}^* = 0$). We define the ellipticity angle of each mode (γ_{QO} and γ_{QX}) as

$$\frac{1}{\tan\gamma_{\text{QO}}} = \frac{iE_{\xi(\text{QO})}}{E_{\eta(\text{QO})}} = \frac{2\cos\theta}{c(\sin^2\theta - \rho)} \tag{8}$$

$$\frac{1}{\tan\gamma_{\text{QX}}} = \frac{iE_{\xi(\text{QX})}}{E_{\eta(\text{QX})}} = \frac{2\cos\theta}{c(\sin^2\theta + \rho)} \tag{9}$$

[1]Strictly speaking, the propagation modes are termed ordinary (O) and extraordinary (X) only for perpendicular propagation ($N_z = 0$). An electrostatic solution, not considered here, is also found for propagation along the magnetic field (Landau plasma oscillations).

Since both modes are orthogonal ($\tan\gamma_{\mathrm{QO}} \equiv -(\tan\gamma_{\mathrm{QX}})^{-1}$), they have opposite polarization sense and inverse ellipticity and thus, only one ellipticity angle is needed. We choose this angle to be $\gamma \equiv \gamma_{\mathrm{QO}}$ with $-\pi/4 \leqslant \gamma \leqslant \pi/4$. We see from (8) that the sign of γ and therefore the polarization rotation sense of the QO–mode in respect to $\mathbf{k}$ is inverted when θ goes from $\theta < \pi/2$ to $\theta > \pi/2$. In this way, the rotation sense *in respect to the magnetic field direction* is the same independently of the value of θ. The same statement is valid for the QX–mode. With the previous choice for γ, the resultant rotation sense of each mode in respect to $\mathbf{k}$ is shown in table 1. The typical polarization ellipses of both modes, for oblique propagation with $\theta > \pi/2$, are represented in figure 5b.

$\gamma < 0 \Leftrightarrow \theta < \frac{\pi}{2}$	$\gamma > 0 \Leftrightarrow \theta > \frac{\pi}{2}$
$\frac{iE_{\xi(\mathrm{QO})}}{E_{\eta(\mathrm{QO})}} < 0$ (L)	$\frac{iE_{\xi(\mathrm{QO})}}{E_{\eta(\mathrm{QO})}} > 0$ (R)
$\frac{iE_{\xi(\mathrm{QX})}}{E_{\eta(\mathrm{QX})}} > 0$ (R)	$\frac{iE_{\xi(\mathrm{QX})}}{E_{\eta(\mathrm{QX})}} < 0$ (L)

Table 1: Mode polarization in respect to $\mathbf{k}$ for $\theta < \pi/2$ and $\theta > \pi/2$.

No details about the longitudinal component of the wave that develops in a plasma will be discussed here since it vanishes in the $\omega_p \to 0$ limit, where the wave coupling to the plasma occurs. Once a proper coupling is achieved, the quality of the mode remains approximately unchanged if the WKB approximation holds along the wave propagation trajectory.

3 Wave polarization in the launching reference system

In the wave reference system (ξ, η, ζ) introduced in the previous section the major axis of the QO–mode transverse polarization ellipse is always parallel to the ξ direction, i.e. the "horizontal" direction in the wave reference system. Similarly, the major axis of the QX–mode ellipse is always parallel to the vertical direction of the wave reference system. For practical purposes, it is very convenient to define the wave polarization in the reference system defined by the vectors $\mathbf{v}$, $\boldsymbol{\epsilon}_w$ and $\mathbf{Z}$. This latter system is related to the orientation of the plane of the power injection window in each sector since $\mathbf{Z}$ is the vertical direction and $\boldsymbol{\epsilon}_w$ is a vector in the horizontal plane directed perpendicularly to the beam launching direction ($\mathbf{v}$) which therefore lies in the window plane (see figures 7 and 9a). In this system (from now on, *the launching reference system*), the major axis of the polarization ellipse is no longer directed along the horizontal direction and an extra rotation angle is needed to describe the wave polarization.

In general, the vacuum field complex amplitude of a plane wave can always be written as

$$\mathbf{E} = a_1 \exp(i\delta_1)\boldsymbol{\epsilon}_1 + a_2 \exp(i\delta_2)\boldsymbol{\epsilon}_2 \tag{10}$$

where a_1, a_2, δ_1 and δ_2 are real quantities and vector $\boldsymbol{\epsilon}_1$ is perpendicular to vector $\boldsymbol{\epsilon}_2$. The polarization ellipse and the two angles ψ and χ that define a general polarization state are represented in figure 6.

The relation between the parameters $a_1, a_2, \delta_1, \delta_2$ that appear in (10) and the angles ψ and χ is given by (11).

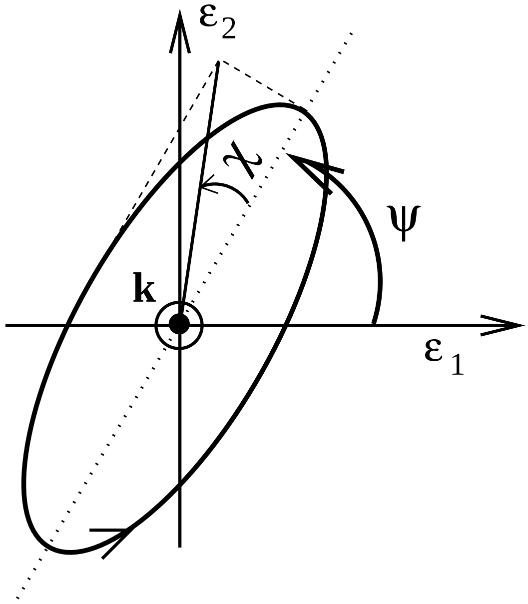

Figure 6: General polarization ellipse (right-handed case is represented in the figure).

$$\begin{aligned} s_1 &= \frac{1-r^2}{1+r^2} = \cos 2\chi \cos 2\psi \\ s_2 &= \frac{2r\cos\delta}{1+r^2} = \cos 2\chi \sin 2\psi \\ s_3 &= \frac{2r\sin\delta}{1+r^2} = \sin 2\chi \end{aligned} \tag{11}$$

where $r \equiv a_2/a_1$, $\delta \equiv \delta_2 - \delta_1$ and s_1, s_2, s_3 are the Stokes parameters of the polarization [8]. The angle ψ is termed the azimuth of the polarization ellipse ($0 \leqslant \psi \leqslant \pi$) and, as in the previous section, χ is its ellipticity angle ($-\pi/4 \leqslant \chi \leqslant \pi/4$). As we have mentioned in the introduction, both heating systems (ECRH & EBW) need an internal mirror to achieve the final launching direction. The wave polarization is changed by the reflection on the mirror surface and this has to be taken into account in the calculation of the final polarization angles. The reflection at the mirror surface and the relation between the different reference systems used in the calculation of the azimuth and the ellipticity angle is illustrated in figure 7. The different vectors represented in the figure are given by

$$
\begin{aligned}
\mathbf{n} &\equiv \frac{\mathbf{u}\times\mathbf{v}}{|\mathbf{u}\times\mathbf{v}|} & \boldsymbol{\epsilon}_i &\equiv \mathbf{n}\times\mathbf{v} \\
& & \boldsymbol{\epsilon}_r &\equiv \mathbf{n}\times\mathbf{u} \\
\mathbf{B} \equiv \mathbf{B} - \mathbf{B}_{\|} &\equiv \mathbf{B} - (\mathbf{u}\cdot\mathbf{B})\mathbf{u} & \boldsymbol{\epsilon}_w &\equiv \mathbf{Z}\times\mathbf{v}
\end{aligned} \tag{12}
$$

where, as mentioned above, $\mathbf{v}$ is the launching direction, $\mathbf{u}$ is the beam direction after the reflection at the internal mirror surface and $\mathbf{B}$ is the magnetic field *at the plasma boundary* along the reflected beam direction. The vectors $\mathbf{u}$ and $\mathbf{B}$ depend on the mirror positioning angles (see Appendix A). All vector components are referred to the main system (X, Y, Z) of the device. By definition, $\mathbf{n}$ is perpendicular to the plane of incidence of the wave ($\mathbf{P}$) and $\mathbf{B}_\perp$ and $\mathbf{n}$ are both perpendicular to $\mathbf{u}$.

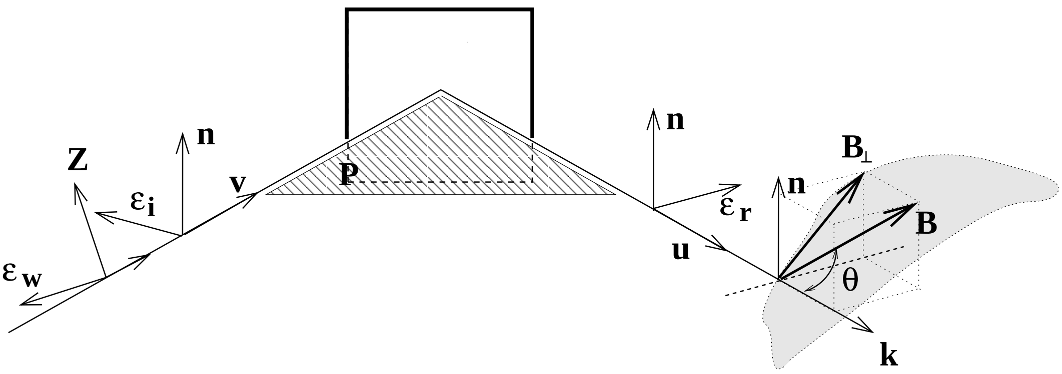

Figure 7: Wave reflection at the internal mirror surface. The plane $\mathbf{P}$ is the incidence plane of the wave. $\mathbf{Z}$ is the vertical direction. The definitions of the other vectors are given in the text.

According to (11), the change in the sign of the perpendicular amplitude [2] introduces a change in the sign of r and therefore a sign reversal of the two last Stokes parameters that define the reflected wave, s_2^r and s_3^r. Therefore

$$s_2^r = -s_2^i = -\cos 2\chi^i \sin 2\psi^i = \cos 2\chi^r \sin 2\psi^r \tag{16}$$

$$s_3^r = -s_3^i = -\sin 2\chi^i = \sin 2\chi^r \tag{17}$$

and thus the relation between the polarization angles of the reflected and the incident waves in the

[2] The complex amplitudes of both incident (i) and reflected (r) fields can be written in each local wave reference system ($\boldsymbol{\epsilon}_i, \mathbf{n}, \mathbf{u}$ and $\boldsymbol{\epsilon}_r, \mathbf{n}, \mathbf{v}$) as

$$\mathbf{E}^i = a_1^i \exp(i\delta_1^i)\boldsymbol{\epsilon}_i + a_2^i \exp(i\delta_2^i)\mathbf{n} \tag{13}$$

$$\mathbf{E}^r = a_1^r \exp(i\delta_1^r)\boldsymbol{\epsilon}_r + a_2^r \exp(i\delta_2^r)\mathbf{n} \tag{14}$$

For of a perfect metallic conductor, only the component perpendicular to the incidence plane (that is, the component along $\mathbf{n}$) changes its sign (or changes its phase by a factor π) whereas the component of the wave field which is parallel to $\mathbf{P}$ is not modified [8]. That is

$$a_1^r = a_1^i \qquad a_2^r = -a_2^i \tag{15}$$

range defined for such angles is given by

$$\chi^r = -\chi^i \tag{18}$$

$$\psi^r = \pi - \psi^i \tag{19}$$

Note that the rotation sense of the polarization ellipse becomes the opposite whereas the sum of both azimuths is always π.

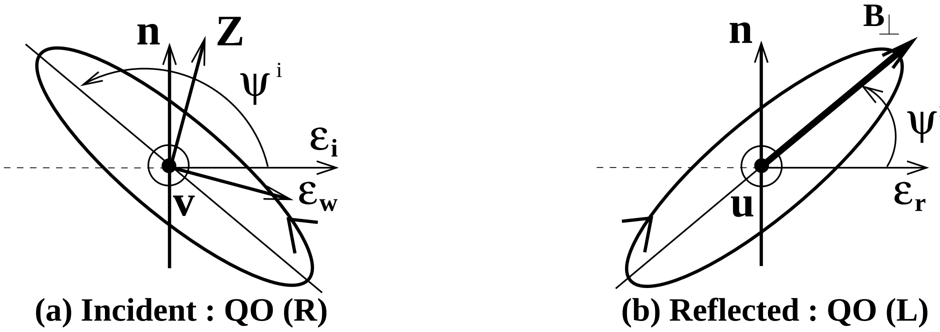

Figure 8: QO–mode polarization ellipse before reflection in the incident system (a) and after reflection in the reflected wave reference system (b). In this particular case, $\theta < \pi/2$. For $\theta > \pi/2$, the QO–mode is right-handed *after* the reflection.

The effect of reflection on wave polarization is illustrated in figure 8. To determine the azimuth of the QO–mode polarization ellipse in the launching system we need first the components of $\mathbf{b}_\perp \equiv \mathbf{B}_\perp/|\mathbf{B}_\perp|$ in the reflected wave system and the components of $\mathbf{Z}$ and $\boldsymbol{\epsilon}_w$ in the incident wave system. These are given by

$$\begin{array}{lll} \widetilde{b}_\perp^{\,1} \equiv \mathbf{b}_\perp \cdot \boldsymbol{\epsilon}_r & \widetilde{Z}^{\,1} \equiv \mathbf{Z} \cdot \boldsymbol{\epsilon}_i & \widetilde{\epsilon}_w^{\,1} \equiv \boldsymbol{\epsilon}_\mathbf{w} \cdot \boldsymbol{\epsilon}_i \\ \widetilde{b}_\perp^{\,2} \equiv \mathbf{b}_\perp \cdot \mathbf{n} & \widetilde{Z}^{\,2} \equiv \mathbf{Z} \cdot \mathbf{n} & \widetilde{\epsilon}_w^{\,2} \equiv \boldsymbol{\epsilon}_\mathbf{w} \cdot \mathbf{n} \\ \widetilde{b}_\perp^{\,3} \equiv 0 & \widetilde{Z}^{\,3} \equiv 0 & \widetilde{\epsilon}_w^{\,3} \equiv 0 \end{array} \tag{20}$$

To include the effect of reflection in the determination of $\psi_{\rm QO}$ we note that the major axis of the polarization ellipse *before* the reflection must coincide with the direction given by the vector $\widetilde{\mathbf{b}}'_\perp \equiv (\widetilde{b}_\perp^{\,1}, -\widetilde{b}_\perp^{\,2}, 0)$. Actually, since only the direction of $\widetilde{\mathbf{b}}'_\perp$, which determines the magnetic field plane, is relevant, we may define a new vector

$$\widehat{\mathbf{b}}_\perp = \begin{cases} +\widetilde{\mathbf{b}}'_\perp & \text{if } \beta > 0 \\ -\widetilde{\mathbf{b}}'_\perp & \text{if } \beta < 0 \end{cases} \tag{21}$$

where $\beta \equiv \cos(\widetilde{\mathbf{Z}} \cdot \widetilde{\mathbf{b}}'_\perp)$. With this definition, the projection of $\widehat{\mathbf{b}}_\perp$ along $\widetilde{\mathbf{Z}}$ is always positive and the azimuth of the QO–mode polarization ellipse is simply given by

$$\boxed{\psi_{\rm QO} = \arccos(\widetilde{\boldsymbol{\epsilon}}_w \cdot \widehat{\mathbf{b}}_\perp)} \tag{22}$$

Since both the QO–mode and the QX–mode are orthogonal, the azimuth of the QX–mode polarization ellipse is inmediately obtained

$$\boxed{\psi_{\rm QX} = \begin{cases} \psi_{\rm QO} + \pi/2 & \text{if } \psi_{\rm QO} < \pi/2 \\ \psi_{\rm QO} - \pi/2 & \text{if } \psi_{\rm QO} > \pi/2 \end{cases}} \tag{23}$$

The above calculation is valid for any **v**, **u**, **B** and **Z** provided that $\mathbf{v} \perp \mathbf{Z}$. In TJ–II, this last condition is fulfilled by all the launched microwave beams.

The ellipticity angle is calculated using (8) and taking into account the change in the rotation sense due to the reflection at the mirror surface. From (8) we know that

$$\tan\gamma = \frac{c(\sin^2\theta - \rho)}{2\cos\theta} \tag{24}$$

Using the identity $\sin^2\gamma + \cos^2\gamma = 1$ in (24) and using the result given by (6) we may write

$$\cos\gamma = \sqrt{\frac{\rho + \sin^2\theta}{2\rho}} \tag{25}$$

$$\sin\gamma = \mathrm{sgn}(\theta - \frac{\pi}{2})\sqrt{\frac{\rho - \sin^2\theta}{2\rho}} \tag{26}$$

Finally, and considering now the reflection at the mirror surface, we obtain

$$\boxed{\chi_{\mathrm{QO}} = -\gamma \qquad \chi_{\mathrm{QX}} = +\gamma} \tag{27}$$

3.1 The 53.2 GHz ECRH system

As we mentioned in the introduction, both quasi-optical transmission lines are located at stellarator symmetric positions[3] and therefore the wave polarization in one line is directly related to the wave polarization in the other line.

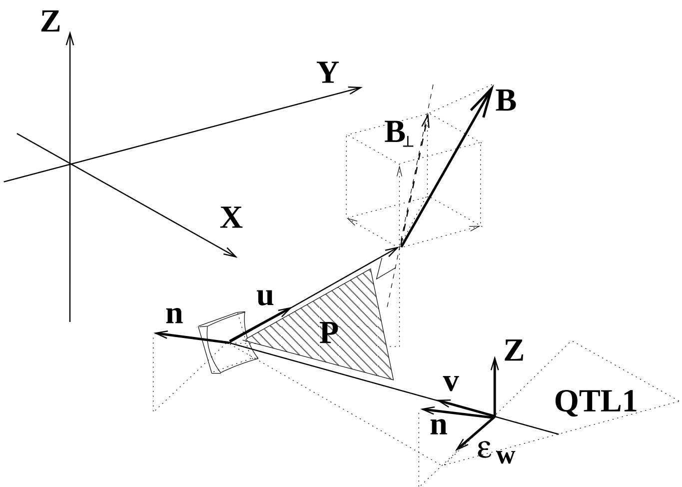

(a)

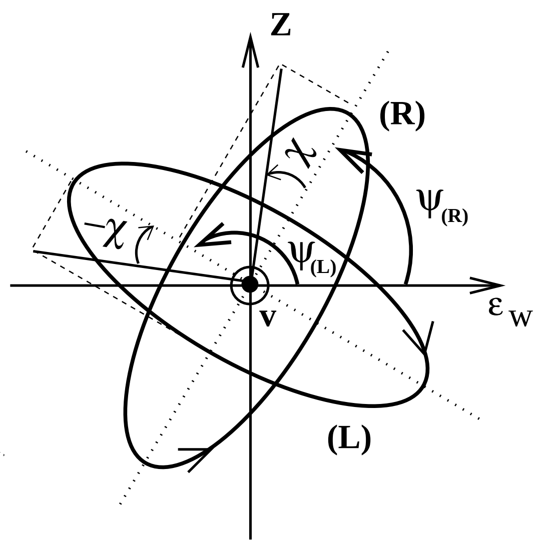

(b)

Figure 9: Geometrical layout of the ECRH power launching in the QTL1 case (a). General polarization ellipses of both orthogonal modes in the reference system defined by $\boldsymbol{\epsilon}_w, \mathbf{Z}$ and $\mathbf{v}$ (b).

Figure 9 shows the geometrical layout in the QTL1 case and the polarization ellipses of both modes. All the variables represented in the figure keep their previous meaning. The linkage between

[3]The stellator symmetry in TJ–II is such that $\psi(r, \pi/4+\varphi, z) = \psi(r, \pi/4-\varphi, -z)$ where ψ stands for the magnetic flux (not to be confused with the azimuth of the polarization ellipse), and r, φ, z are the usual cylindrical coordinates.

the QO and QX modes coupled to the plasma and the launched R and L modes depends on whether the propagation angle θ is larger or smaller than $\pi/2$ and the result is modified in respect to table 1 due to the reflection at the mirror surface (see table 2). The polarization angles that are needed to couple a QO or a QX–mode at the plasma boundary and their dependence on the launching direction, for power injection on-axis, are represented in figures 10 and 11. The propagation angle (θ) and the field at the boundary are also shown. Due to the stellarator symmetric position of both lines, $\psi_{\rm QO}$ at a given $N_\parallel$ in one line is equal to $\psi_{\rm QO}$ at $-N_\parallel$ in the other line. In respect to the ellipticity angle, $\chi_{\rm QO}$ at a given $N_\parallel$ in one line is equal to $-\chi_{\rm QO}$ at $-N_\parallel$ in the other line. The same is valid for the QX–mode polarization.

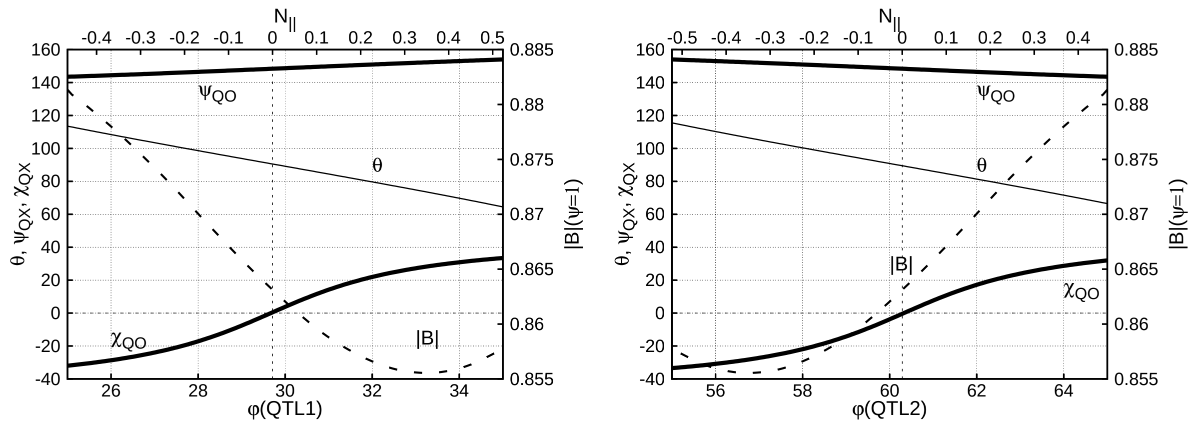

Figure 10: Launched wave polarization angles needed to couple a QO–mode at the plasma boundary, for different injection positions along the magnetic axis. Both lines are represented (QTL1 on the left and QTL2 on the right).

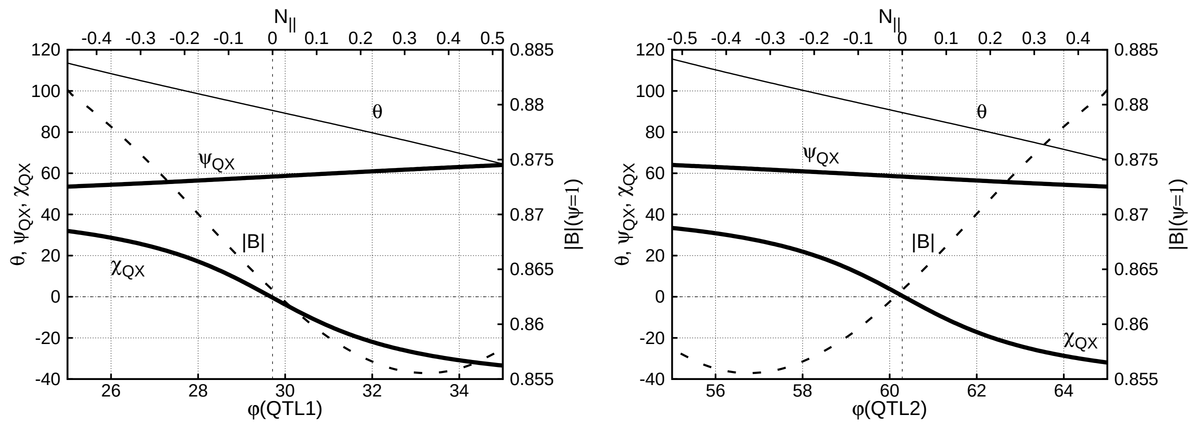

Figure 11: Dependence of the launched wave polarization angles on the launching direction for QX–mode coupling at the plasma boundary.

In these figures, the launching direction is determined by the TJ–II toroidal angle (φ) for which the axis of the launched beam in vacuum intersects the magnetic axis and also by the value of the parallel refraction index ($N_\parallel = (c/\omega|\mathbf{B}|)\mathbf{k}\cdot\mathbf{B}$) in vacuum calculated along the magnetic axis. The calculation has been performed for the standard 100_40_63 magnetic configuration. Table 2 shows the polarization angles in each line for some values of $N_\parallel$ on-axis. Note that for $N_\parallel = 0$, the propagation angle at the boundary (θ) is not exactly 90° but 89.5° in QTL2 and 90.5° in QTL1.

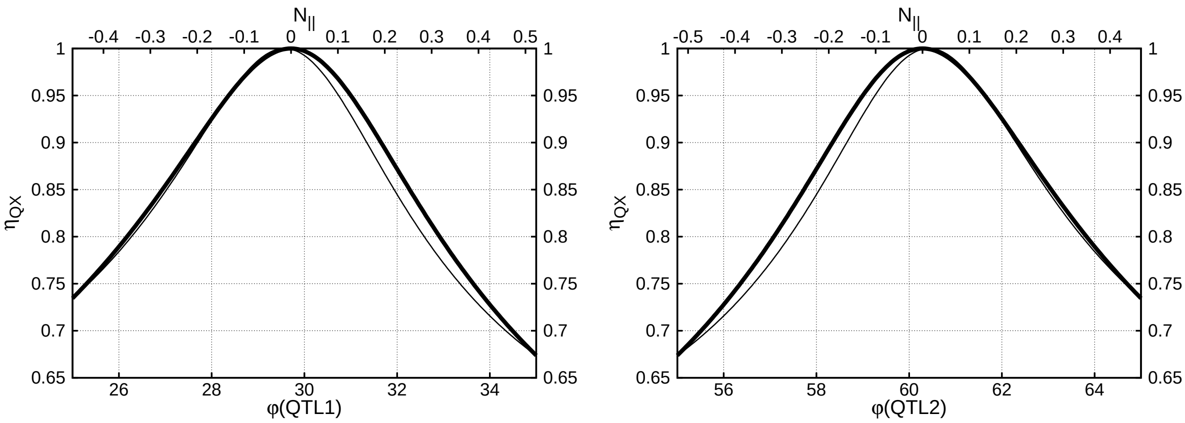

Figure 12: Dependence of the power coupled to the QX–mode on the launching direction given by φ (thin line) and alternatively by $N_{\|}$ (thick line). Note the non linear relationship between φ and $N_{\|}$ because of the 3-D magnetic axis. Within the available range of the internal launchers, the minimum power coupled to the X–mode in non matched conditions is of the order of 70%.

The dependence of the positioning angles of both internal mirrors on the TJ–II toroidal angle φ and the parallel index $N_{\|}$ is summarized in Appendix A.

QTL1				**QTL2**			
$N_{\|}$	θ	$\psi_{\rm QO}$	$\chi_{\rm QO}$	$N_{\|}$	θ	$\psi_{\rm QO}$	$\chi_{\rm QO}$
−0.4	110.3	144.1	−29.8	−0.4	109.0	152.6	−29.2
−0.2	100.3	146.2	−19.4	−0.2	99.1	150.3	−17.9
0.0	90.5	148.2	−1.2	0.0	89.5	148.2	+1.2
+0.2	80.9	150.3	+17.9	+0.2	79.7	146.2	+19.4
+0.4	71.0	152.6	+29.2	+0.4	69.7	144.1	+29.8

Table 2: QO–mode polarization and propagation angles for some values of $N_{\|}$ on-axis. The values for perpendicular injection are highlighted. Complete tables for both lines appear in Appendix B.

As shown in table 2, the nominal linear polarization for perpendicular injection is not the appropriate one for ECCD and ECRH experiments with oblique injection. In this case, the optimum QX–mode polarization is not linear and the use of a constant linear polarization precludes perfect matching. If the nominal linear polarization is not modified, the amount of power in the QX–mode for non perpendicular injection along the axis is given by

$$\eta_{\rm QX} = \frac{1}{2}(1 + \mathbf{s}_{\rm QX} \cdot \mathbf{s}_{\rm X}) \tag{28}$$

where $\mathbf{s}_{\rm X}$ is the Stokes vector of the linear X–mode polarization for perpendicular injection and $\mathbf{s}_{\rm QX}$ is the Stokes vector of the elliptical QX–mode polarization. The dependence of $\eta_{\rm QX}$ on the launching direction (φ and $N_{\|}$ on–axis) in both lines is plotted in figure 12.

3.2 The 28 GHz EBW system

3.2.1 EBW heating system

The O–X–B mode conversion scenario needs a very precise injection angle in order to achieve the full O–X conversion efficiency of the QO–mode launched wave. The launching configuration and the corresponding **v**, **u**, and **B** vectors in this case appear in figure 13. Also, in figure 13 (a), the polarization ellipse in the launching reference system, at the output of the 28 GHz power injection waveguide, is represented. Using here the same method that was developed in section 3, we find that the polarization angles for the optimum theoretical position are

$$\boxed{\psi_{\mathrm{QO}} = 176.2^\circ \qquad \chi_{\mathrm{QO}} = -34.9^\circ} \tag{29}$$

Because we are pursuing an O–X mode conversion, the optimum launching direction depends on the density profile. The result presented in (29) has been obtained for $n_e = 1.7(1-\psi^{1.375})^{1.5} \times 10^{19}$ m^{-3} in a standard magnetic field configuration (100_40_63). For these conditions, an optimum theoretical direction was determined in [9]. This direction ensures an optimum parallel refraction index ($N_{||}^{opt} = \sqrt{Y/(1+Y)}$, where $Y \equiv \omega_c/\omega$) at the QO–mode cutoff layer (where $\omega_p^2 = \omega^2$) and therefore a maximum O–X conversion efficiency. The values given by (29) are the ones needed to couple the QO–mode at the plasma boundary for this launching direction. A deviation from the optimum injection position (for given constant profiles) causes a reduction of the O–X transmission efficiency and needs also a correction of the launched wave polarization to avoid further degradation of the conversion efficiency. The left panel of figure 14 shows the O–X mode conversion efficiency when the launching direction is modified. The dependence of the QO–mode polarization content on the polarization angles of the injected radiation is also shown. For $\psi = \psi_{\mathrm{QO}} - 90^\circ$ and $\chi = -\chi_{\mathrm{QO}}$ all the power is launched in the X mode. In addition, figure 15 shows the optimum polarization angles for each launching direction. The spatial location of the QO–mode cutoff depends on the density profile and therefore the magnetic field experienced by the wave at the QO–mode cutoff may change. Thus, each density profile has its own optimum launching direction and its own optimal wave polarization.

3.2.2 EBE detection system

Again, a similar calculation to the one performed above but using now $\mathbf{v}'$ and $\mathbf{Z}'$ (see figure 13) allows us to determine the polarization angles of the incident wave before the reflection at the internal elliptical mirror, *as if it were launched from the detection antenna.* Both vectors are obtained from the former **v** and **Z** by a rotation of angle $\alpha = 20^\circ$ around the $\boldsymbol{\epsilon}_w$ axis and therefore $\mathbf{v}' \perp \mathbf{Z}'$. This value of α is the design value for which the radiation collected from the plasma, looking along the optimum O–X conversion direction, is perfectly reflected (in the **Z** direction) towards the detection antenna. In this case, the polarization angles of the *forward* wave, represented in figure 13 (b) are

$$\psi'_{\mathrm{QO}} = 9.9^\circ \qquad \chi'_{\mathrm{QO}} = -34.9^\circ \tag{30}$$

Obviously, $\chi'_{\mathrm{QO}} = \chi_{\mathrm{QO}}$ since **u** and **B** are always the same vectors corresponding to the optimum O–X conversion.

If we now take into account the reflection at the plane mirror of the detection system, the polarization of the wave incident upon this mirror, given in the antenna detection system shown in figure 13 (c) is determined by applying (18) and (19) to (30)

$$\psi''_{\mathrm{QO}} = 170.1^\circ \qquad \chi''_{\mathrm{QO}} = +34.9^\circ \tag{31}$$

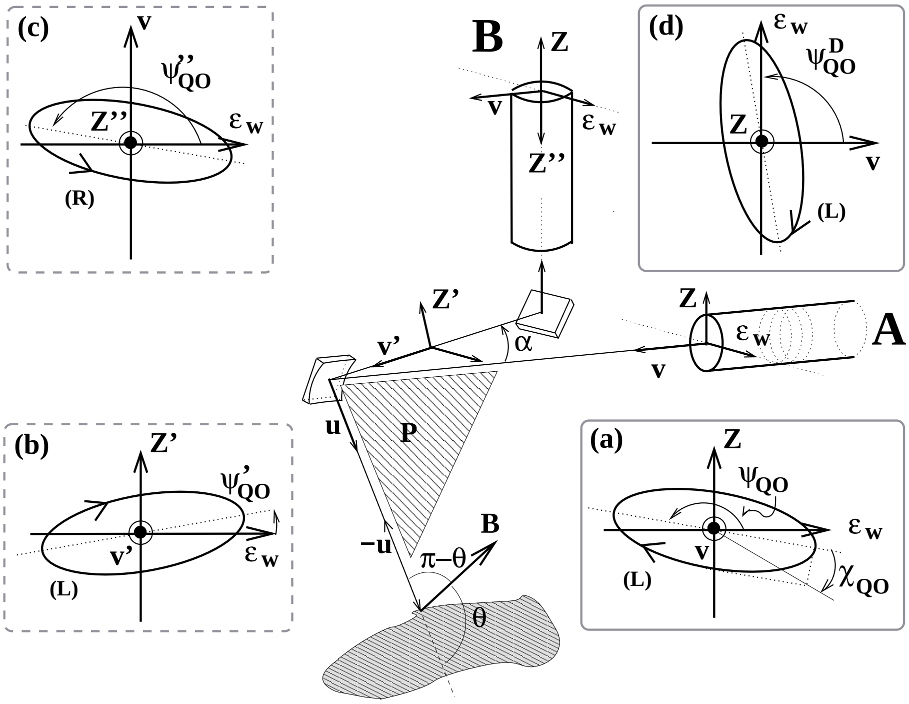

Figure 13: Geometrical layout of the EBW launching (A) and detection (B) systems. The polarization ellipses of the high power launched wave (a) and the polarization ellipse of the *emitted* wave at the detection antenna (d) are shown. Intermediate steps of the detected wave polarization calculation are also shown ((b) and (c).)

where now $\chi''_{\rm QO} = -\chi'_{\rm QO}$ since, as we have seen above, the reflection changes the polarization rotation sense.

These are the angles to couple a QO–mode wave if the power were to be launched through the detection antenna. Since we are interested in the polarization of the *emitted* wave, we must take into account that the propagation angle in respect to **B** changes from θ to $\pi - \theta$ and therefore the sign of the ellipticity angle is reversed. The final polarization angles of the emitted wave detected at the antenna in the reference system illustrated in figure 13 (d) are

$$\boxed{\psi^D_{\rm QO} = 99.9^\circ \qquad \chi^D_{\rm QO} = -34.9^\circ} \tag{32}$$

EBE experiments were performed in NBI plasmas [10] making use of the detection antenna (a quad-ridged dual polarized microwave horn). To this end, the horn was rotated around its axis $\boldsymbol{Z''}$. The results obtained were consistent with the expected polarization of the B-X-O emitted wave.

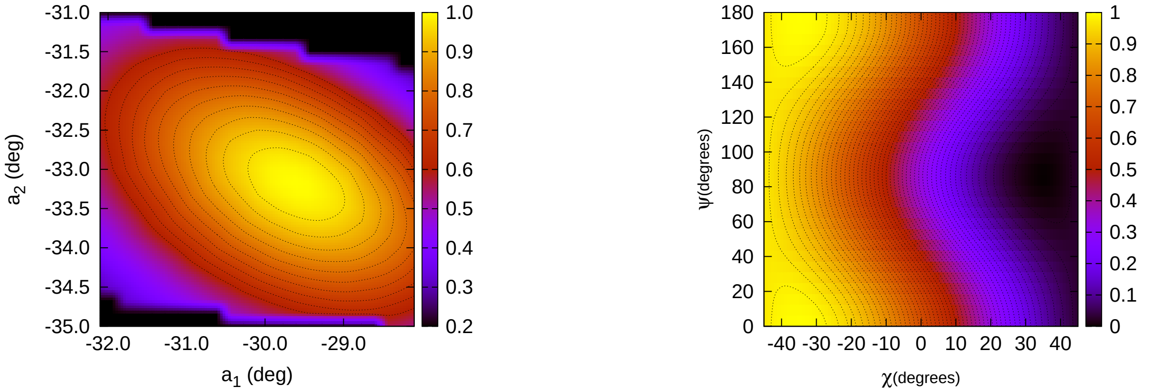

Figure 14: On the left, the dependence of the O–X mode conversion efficiency on the EBW mirror positioning angles for the density profile given above. The optimum mode conversion is obtained when $a_1 \equiv a_1^{opt} = -29.6°$ and $a_2 \equiv a_2^{opt} = -33.2°$. The right viewgraph shows the dependence of the QO mode content of the injected radiation on the wave polarization angles for the optimum launching direction.

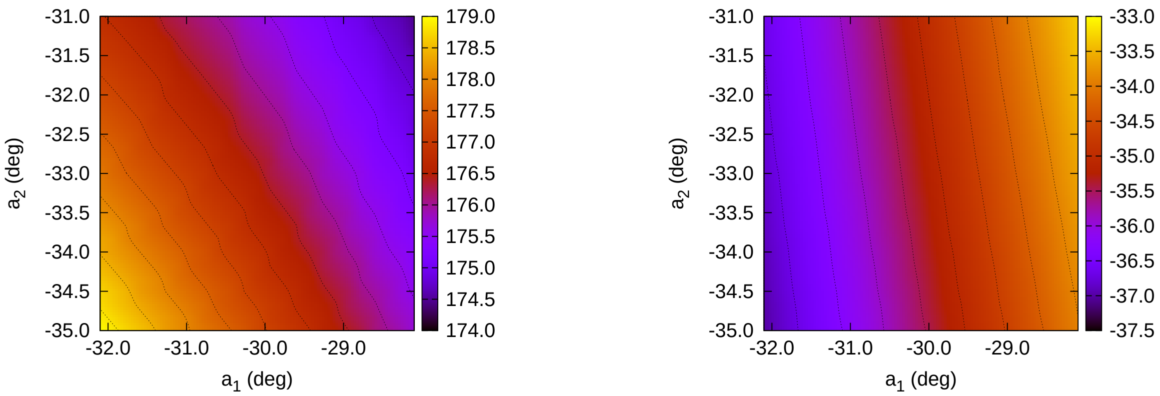

Figure 15: Optimum azimuth (left) and ellipticity angle (right) of the polarization ellipse for different orientations of the internal mirror. Only small variations (maximum 5°) from the optimum angles are needed to match a perfect QO mode across the whole range of launching directions.

4 Wave polarization control

As it has been stated all along this document, launched waves should have a specific polarization in order to obtain the desired results. Modern gyrotrons for ECRH applications in plasmas employ an internal quasi-optical converter with a linearly polarized TEM_{00} (Gaussian) mode output. Thus, to obtain the desired polarization for ECRH and ECCD experiments, the transmission systems are generally equipped with a set of two corrugated polarizers mirrors which are able to provide any desired output polarization from any given input one. In general, when considering low incident angles, the first polarizer (first to receive the wave) has a corrugation depth around $\lambda/8$, where λ is the wavelength ($\lambda_{28} = 10.71$ mm, $\lambda_{53.2} = 5.64$ mm) and varies the ellipticity of the polarization ellipse whereas the second mirror uses a corrugation depth of approximately $\lambda/4$ and rotates the major axis of the polarization ellipse. Additionally to this polarization control system, non desired changes in the polarization may also be introduced by waveguide bends, particularly when the output desired polarization is elliptical and several non coplanar bends are used in the transmission system, as it occurs in TJ–II for the 28 GHz case. Therefore, all those additional effects should be accounted for in order to provide an output polarization from the polarizers which leads to the desired wave out from the waveguide.

In the following, the theoretical behaviour of polarizers mirrors and bends is briefly outlined and the results for the two TJ–II ECRH systems are presented.

4.1 Grooved mirror polarizers

The carving of grooves in the surface of plane mirrors makes the anisotropic reflective surface of the plane mirror become direction and polarization dependent. In order to make a rigorous analysis of the reflection from a grooved mirror the new boundary conditions have to be taken into account. Fig. 16 (taken from [11] and similar to that of [12]) depicts a plane wave with wave vector **k** incident upon a grooved mirror with its grooves along the z direction.

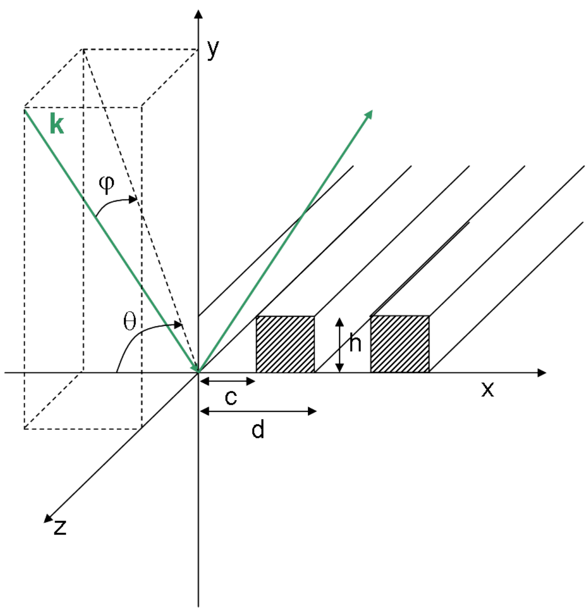

Figure 16: Grooved mirror reference system. **k** is the incident wave vector, φ is the angle between **k** and its projection on the xy plane and θ is the angle between the projection and the x axis.

The $\mathbf{E}$ field from that wave can be represented (assuming an $\exp(-i\omega t)$ temporal variation) as a complex amplitude with an $\exp[i(\alpha_0 x - \beta_0 y + \gamma z)]$ variation with $k^2 = \alpha_0^2 + \beta_0^2 + \gamma^2 = \omega^2\mu\epsilon$ being ω, μ and ϵ the radian frequency, the magnetic susceptibility and the electric permittivity respectively. The electromagnetic field should be then decomposed into two orthogonal fields: the fast polarization field ($\mathbf{E_f}$), in which the H_z field component nullifies, and the slow polarization ($\mathbf{E_s}$) in which the E_z component is also zero. The reason behind this slow-fast notation arises from the phase difference which each of the two orthogonal components suffers after the reflection on the grooved mirror as it will be clear afterward.

Taking into account an $\exp(i\gamma z)$ field variation along the z direction and source free Maxwell equations

$$\nabla \times \mathbf{E} = \quad i\omega\mu\mathbf{H} \tag{33a}$$
$$\nabla \times \mathbf{H} = -i\omega\epsilon\,\mathbf{E} \tag{33b}$$

the different electromagnetic field components can be obtained as

$$E_x = \frac{i\gamma}{a^2}\frac{\partial E_z}{\partial x} + \frac{i\omega\mu}{a^2}\frac{\partial H_z}{\partial y} \tag{34a}$$
$$E_y = \frac{i\gamma}{a^2}\frac{\partial E_z}{\partial y} - \frac{i\omega\mu}{a^2}\frac{\partial H_z}{\partial x} \tag{34b}$$
$$H_x = \frac{i\gamma}{a^2}\frac{\partial H_z}{\partial x} - \frac{i\omega\epsilon}{a^2}\frac{\partial E_z}{\partial y} \tag{34c}$$
$$H_y = \frac{i\gamma}{a^2}\frac{\partial H_z}{\partial y} + \frac{i\omega\epsilon}{a^2}\frac{\partial E_z}{\partial x} \tag{34d}$$

where $a^2 = k^2 - \gamma^2$ and which directly depend on the longitudinal components.

The next step is to obtain the solution for each one of the two orthogonal components of the field. For this to be done, two regions can be recognized in the solution of the problem: the region outside the grooves ($y \geq h$) and the region inside the grooves ($0 \leq y \leq h$).

Beginning with the outer region, the field for fast and slow polarization components can be obtained. Both fields must satisfy the scalar wave equation, namely

$$\nabla^2 u + k^2 u = 0 \tag{35}$$

From [13] we know that the solution in the outer region can be written by means of the Rayleigh expansion as

$$u(x,y,z) = \exp[i(\alpha_0 x - \beta_0 y + \gamma z)] + \sum_{n=-\infty}^{\infty} r_n \exp[i(\alpha_n x + \beta_n y + \gamma z)] \tag{36}$$

with r_n being unknown coefficients and

$$\alpha_n = \alpha_0 + 2\pi\frac{n}{d} \tag{37a}$$
$$\beta_n = \left(k^2 - \alpha_n^2 - \gamma^2\right)^{\frac{1}{2}} \tag{37b}$$

In this expression the single term can be identified as the incident field and the summation represents the total reflected and diffracted field after the mirror. Consequently, the z components of the fast and slow fields can be written as

$$E_{zf}(x,y,z) = C_f \left\{ \exp\left[i\left(\alpha_0 x - \beta_0 y + \gamma z\right)\right] + \sum_{n=-\infty}^{\infty} r_n \exp\left[i\left(\alpha_n x + \beta_n y + \gamma z\right)\right] \right\} \tag{38a}$$

$$H_{zf}(x,y,z) = 0 \tag{38b}$$

$$E_{zs}(x,y,z) = 0 \tag{38c}$$

$$H_{zs}(x,y,z) = C_s \left\{ \exp\left[i\left(\alpha_0 x - \beta_0 y + \gamma z\right)\right] + \sum_{n=-\infty}^{\infty} s_n \exp\left[i\left(\alpha_n x + \beta_n y + \gamma z\right)\right] \right\} \tag{38d}$$

being C_f and C_s two arbitrary complex constants and r_n and s_n being unknown coefficients. With these z components, the x and y components of the fast and slow polarizations can be obtained using eqs. (34a),...,(34d).

After the outer field has been determined, the field inside the grooves must be derived. Considering the fast polarization, the scalar wave equation (35) must be solved and solutions must also fulfill the boundary conditions, i.e. $E_z(x,y,z) = 0$ at $x = 0$, $x = c$ and $y = 0$, for the region between grooves. In order to solve the wave equation, a modal expansion can be made which, taking into account the boundary conditions, leads to the next equation:

$$E_z(x,y,z) = \begin{cases} \displaystyle\sum_{n=1}^{\infty} a_n \sin\left(\tfrac{n\pi x}{c}\right) \sin\left(A_n y\right) \exp\left(iz\gamma\right) & 0 \le x \le c \\ 0 & c < x \le d \end{cases} \tag{39}$$

where $A_n^2 = a^2 - (n\pi/c)^2$. The term $\sin(A_n y)$ is replaced by $\sinh\left(\overline{A_n} y\right)$ if

$$a^2 - \left(\frac{n\pi}{c}\right)^2 < 0, \qquad \overline{A_n} = \left[\left(\frac{n\pi}{c}\right)^2 - a^2\right]^{1/2} \tag{40}$$

Although the same wave equation is to be solved, the boundary conditions change for the slow polarization problem when solving for H_z. In this case, the conducting walls impose $\partial H_z/\partial x = 0$ at $x = 0$, $x = c$ and $\partial H_z/\partial y = 0$ at $y = 0$. Hence, taking into account these boundary conditions, and performing a modal expansion as above, the solutions results:

$$H_z(x,y,z) = \sum_{n=0}^{\infty} b_n \cos\left(\frac{n\pi x}{c}\right) \cos\left(B_n y\right) \exp\left(iz\gamma\right), 0 \le x \le c \tag{41}$$

where $B_n^2 = a^2 - (n\pi/c)^2$. The term $\cos(B_n y)$ is replaced by $\cosh\left(\overline{B_n} y\right)$ if

$$a^2 - \left(\frac{n\pi}{c}\right)^2 < 0, \qquad \overline{B_n} = \left[\left(\frac{n\pi}{c}\right)^2 - a^2\right]^{1/2} \tag{42}$$

Once the general expressions for the fields have been obtained for the inner and outer regions, in order to get the r_n, s_n, a_n and b_n coefficients, tangential fields have to be matched at the interface $(y = h)$. Considering first the fast polarization case, (in which $H_z = 0$) the following conditions can be imposed for the interface:

a. Continuity for $E_z(x,y,z)|_{y=h}$ when $0 \le x \le d$,

b. Continuity for $H_x(x,y,z)|_{y=h}$ when $0 \le x \le c$.

As [12] details (specially in the appendix), if the nth Fourier coefficients of the functions are calculated and then equaled, these continuity conditions lead to two coupled equations which can be solved to obtain the r_n and a_n coefficients:

$$\frac{a^2}{k^2}\left[\delta_{n0}\exp\left(-i2\beta_0 h\right)+r_n\right]=\sum_{m=1}^{\infty}\frac{a_m}{d}\sin\left(A_m h\right)\exp\left(-i\beta_n h\right)I_{nm} \tag{43a}$$

$$\sum_{m=-\infty}^{\infty}\frac{a^2}{k^2}\left[\left(-i\beta_0\right)\delta_{m0}\exp\left(-i\beta_0 h\right)+r_m\left(i\beta_m\right)\exp\left(i\beta_m h\right)\right]c_{n-m}=\frac{1}{d}\sum_{m=1}^{\infty}a_m A_m\cos\left(A_m h\right)I_{nm} \tag{43b}$$

with

$$I_{nm}=\int_0^c \sin\left(\frac{m\pi x}{c}\right)\exp\left(-i\alpha_n x\right)dx=\begin{cases}\frac{m\pi c}{(c\alpha_n)^2-(m\pi)^2}\left[(-1)^m\exp\left(-i\alpha_n c\right)-1\right], & \left(\frac{m\pi}{c}\right)^2\neq\alpha_n^2\\ \frac{-ic}{2}, & \frac{m\pi}{c}=\alpha_n\\ \frac{ic}{2}, & -\frac{m\pi}{c}=\alpha_n\end{cases} \tag{44}$$

and

$$c_n=\begin{cases}\frac{1}{i2\pi n}\left[1-\exp\left(-in2\pi\frac{c}{d}\right)\right] & n\neq 0\\ \frac{c}{d} & n=0\end{cases}$$

Similarly, in case of the slow polarization ($E_z=0$), similar continuity conditions should be met:

a. Continuity for $H_z(x,y,z)|_{y=h}$ when $0 \le x \le c$

b. Continuity for $E_x(x,y,z)|_{y=h}$ when $0 \le x \le d$

which will also lead to another two coupled equations from which the s_n and b_n coefficients can be obtained:

$$\sum_{m=-\infty}^{\infty}\frac{a^2}{k^2}\left[\delta_{m0}\exp\left(-i\beta_0 h\right)+s_m\exp\left(i\beta_m h\right)\right]c_{n-m}=\frac{1}{d}\sum_{m=0}^{\infty}b_m\cos\left(B_m h\right)J_{nm} \tag{45a}$$

$$\frac{a^2}{k^2}\left[\left(-i\beta_0\right)\delta_{n0}\exp\left(-i2\beta_0 h\right)+s_n\left(i\beta_n\right)\right]=\frac{1}{d}\sum_{m=0}^{\infty}\left(-b_m B_m\right)\sin\left(B_m h\right)\exp\left(-i\beta_n h\right)J_{nm} \tag{45b}$$

with

$$J_{nm} = \int_0^c \cos\left(\frac{m\pi x}{c}\right) \exp\left(-i\alpha_n x\right) dx = \begin{cases} \frac{ic^2\alpha_n}{(c\alpha_n)^2-(m\pi)^2}\left[(-1)^m \exp\left(-i\alpha_n c\right) - 1\right], & \left(\frac{m\pi}{c}\right)^2 \neq \alpha_n^2 \\ \frac{c}{2}, & \left(\frac{m\pi}{c}\right)^2 = \alpha_n^2 \end{cases} \tag{46}$$

Although these coefficients can be obtained numerically by taking a high enough number of r_n, s_n, a_n and b_n coefficients for the field to be well described and by solving using matrix arithmetic as described in [12], it is of great importance to get an analytical solution for the usual operation range.

From (37b) and (37a) β_n can be evaluated. For a diffracted mode to be propagating, β_n has to be a real positive number. That is to say that the condition

$$\alpha_n^2 < k^2 - \gamma^2 \tag{47}$$

must be met. Keeping in mind that $a^2 = \omega^2\mu\epsilon - \gamma^2 = k^2 - \gamma^2 = k^2\cos^2\varphi$, the previous condition can be converted into

$$\left|\alpha_0 + n\frac{2\pi}{d}\right| < |k\cos\varphi| \tag{48}$$

which, if we realize that $\alpha_0 = k\cos\theta\cos\varphi$, leads to

$$\left|\cos\theta\cos\varphi + n\frac{\lambda}{d}\right| < |\cos\varphi| \tag{49}$$

with $n\in\mathbb{Z}$, $0 \leq \theta \leq \pi/2$ and $-\pi/2 \leq \varphi \leq \pi/2$. In the usual operation range, the primary concern is the absence of diffracted modes, thus searching for $\alpha_n^2 \geq k^2 - \gamma^2$. Hence, $n = \pm 1$ modes must be evaluated, which leads to the following conditions:

$$\frac{\lambda}{d} \geq \cos\varphi\left(1 - \cos\theta\right), n = \quad 1, \tag{50a}$$

$$\frac{\lambda}{d} \geq \cos\varphi\left(1 + \cos\theta\right), n = -1. \tag{50b}$$

As eq. (50b) is more restrictive than (50a) and for any incident angles, the general condition for the absence of diffracted waves (thus leading to the only existence of r_0 and s_0) is:

$$\frac{\lambda}{d} > 2 \tag{51}$$

When evaluating the modal expansions inside the grooves it is important to realize that for any particular n value, when the conditions (40) and (42) are met (for fast and slow polarizations respectively), there is no propagation of the nth mode, which is instead at cutoff (or evanescent). This can be easily seen if the $\sin\theta = \frac{e^{i\theta}-e^{-i\theta}}{2i}$ and $\sinh\theta = \frac{e^{\theta}-e^{-\theta}}{2}$ trigonometric and hyperbolic expressions and their cosine equivalents are taken into account. As was done before, it is important to keep in mind that $a^2 = k^2 - \gamma^2 = k^2\cos^2\varphi$; then, for both fast and slow polarizations, the cutoff frequency under which each n mode is evanescent can be calculated as

$$f_c = \frac{1}{2\sqrt{\mu\epsilon}}\frac{1}{\cos\varphi}\frac{n}{c}. \tag{52}$$

From this expression, it can be deduced that for $n = 0$ modes the cutoff frequency is 0. Expressions (39) and (41) show that there is no $n = 0$ mode (and therefore no a_0 coefficient) for the fast polarization, as it is canceled, but it exists for the slow polarization. If the expressions for this mode are evaluated:

$$
\begin{aligned}
H_z &= + b_0 \cos\left(B_0 y\right) \exp\left(iz\gamma\right), && \text{(53a)}\\
E_x &= - \frac{i\omega\mu}{a^2} b_0 B_0 \sin\left(B_0 y\right) \exp\left(iz\gamma\right), && \text{(53b)}\\
H_y &= - \frac{i\gamma}{a^2} b_0 B_0 \sin\left(B_0 y\right) \exp\left(iz\gamma\right), && \text{(53c)}
\end{aligned}
$$

it can be deduced that they represent a TEM mode of a parallel plate waveguide which is consistent with the 0 cutoff frequency.

The minimum cutoff frequency for higher order modes and for any incident angle appears when $\gamma = 0$ and for $n = 1$ modes. In that case $\lambda = 2c$. Then, to ensure that no higher order modes are propagating in the grooves, the condition

$$\frac{\lambda}{c} > 2 \qquad (54)$$

should be met. Hence, if (54) is fulfilled, only the TEM mode and no higher order modes are propagating inside the grooves. Therefore, the field can be sufficiently well described using the $n = 0$ mode, which means only the b_0 coefficient will be taken into account.

Finally, this means that if (42) and (54) conditions are satisfied, and therefore only r_0, s_0 and b_0 need to be included, then it is straightforward to evaluate the Rayleigh coefficients as:

$$\boxed{r_0 = - \exp\left(-2i\beta_0 h\right)} \qquad \text{(55a)}$$

$$\boxed{s_0 = \frac{-a\frac{c}{d}\tan\left(ah\right) + i\beta_0}{a\frac{c}{d}\tan\left(ah\right) + i\beta_0} \exp\left(-2i\beta_0 h\right)} \qquad \text{(55b)}$$

Once this coefficients have been obtained, it is time to study the change in the polarization based upon them. Back to (38a), and for the fast polarization, the E_{zf} component of the outer field (where subscript stands for fast polarization) can be expressed as:

$$E_{zf} = C_f \left[\exp\left[i\left(\alpha_0 x - \beta_0 y + \gamma z\right)\right] + r_0 \exp\left[i\left(\alpha_0 x + \beta_0 y + \gamma z\right)\right]\right] \qquad (56)$$

where the incident and reflected waves can be identified. In order to simplify the expressions and gather similar x, y, z dependencies, the following notation will be used:

$$
\begin{aligned}
E_{z^+} =& C_f \exp\left[i\left(\alpha_0 x + \beta_0 y + \gamma z\right)\right] && \text{(57a)}\\
E_{z^-} =& C_f \exp\left[i\left(\alpha_0 x - \beta_0 y + \gamma z\right)\right] && \text{(57b)}
\end{aligned}
$$

leading to

$$E_{zf} = E_{z^-} + r_0 E_{z^+} \qquad (58)$$

where C_f is an arbitrary complex constant whose modulus represents the total z component of the electric field as there is no E_{zs} component.

The rest of the fast polarization components can be obtained using eqs. (34a),...,(34d) taking into account E_{z-} and E_{z+} dependencies for the partial derivatives, leading to:

$$E_{xf} = -\frac{\alpha_0\gamma}{a^2}E_{z^-} - r_0\frac{\alpha_0\gamma}{a^2}E_{z^+} \tag{59a}$$
$$E_{yf} = +\frac{\beta_0\gamma}{a^2}E_{z^-} - r_0\frac{\beta_0\gamma}{a^2}E_{z^+} \tag{59b}$$

Using the same equations and a similar idea for the slow polarization leads to:

$$E_{xs} =\frac{\omega\mu\beta_0}{a^2}H_{z^-} - s_0\frac{\omega\mu\beta_0}{a^2}H_{z^+} \tag{60a}$$
$$E_{ys} =\frac{\omega\mu\alpha_0}{a^2}H_{z^-} + s_0\frac{\omega\mu\alpha_0}{a^2}H_{z^+} \tag{60b}$$
$$E_{zs} =0 \tag{60c}$$

From Maxwell's equations and taking into account the $\exp(-i\omega t)$ temporal variation, we know that $\nabla \times \mathbf{E} = i\omega\mu\mathbf{H}$. Then, calculating for the z component we obtain:

$$\frac{\partial E_y}{\partial x} - \frac{\partial E_x}{\partial y} = i\omega\mu H_z \tag{61}$$

where, as there is no H_z component for fast polarization, $H_z = H_{zs}$. If, similarly as in eqs. (57a) and (57b), the total x and y fields are decomposed in an arbitrary constant and their x, y, z variations, the following notation can be used:

$$E_{x^+} =C_{x^+}\exp\left[i\left(\alpha_0 x + \beta_0 y + \gamma z\right)\right] \tag{62a}$$
$$E_{x^-} =C_{x^-}\exp\left[i\left(\alpha_0 x - \beta_0 y + \gamma z\right)\right] \tag{62b}$$

$$E_{y^+} =C_{y^+}\exp\left[i\left(\alpha_0 x + \beta_0 y + \gamma z\right)\right] \tag{63a}$$
$$E_{y^-} =C_{y^-}\exp\left[i\left(\alpha_0 x - \beta_0 y + \gamma z\right)\right] \tag{63b}$$

When imposing equation (61) over eqs. (60a)...(60c) using this notation, a new set of slow polarization field equations can be obtained:

$$E_{xs} =\frac{\beta_0\alpha_0}{a^2}E_{y^-} + \frac{\beta_0^2}{a^2}E_{x^-} - s_0\frac{\beta_0\alpha_0}{a^2}E_{y^+} + s_0\frac{\beta_0^2}{a^2}E_{x^+} \tag{64a}$$
$$E_{ys} =\frac{\alpha_0^2}{a^2}E_{y^-} + \frac{\alpha_0\beta_0}{a^2}E_{x^-} + s_0\frac{\alpha_0^2}{a^2}E_{y^+} - s_0\frac{\alpha_0\beta_0}{a^2}E_{x^+} \tag{64b}$$
$$E_{zs} =0. \tag{64c}$$

From the (57a), (57b) definitions and their H_z equivalents, we know that

$$E_{z^+} =E_{z^-}\exp\left(2i\beta_0 y\right) \tag{65a}$$
$$H_{z^+} =H_{z^-}\exp\left(2i\beta_0 y\right) \tag{65b}$$

If aditionally equation (61) is used on (65b), the following relationships can be obtained:

$$E_{x^+} = -\,E_{x^-}\,\exp\left(2i\beta_0 y\right) \tag{66a}$$

$$E_{y^+} = +\,E_{y^-}\,\exp\left(2i\beta_0 y\right) \tag{66b}$$

Analyzing eqs. (58), (59a), (59b) and (64a)...(64c); incident and reflected fields can be extracted. Then, writing in matrix form the reflected fields leads to:

$$\mathbf{E_r} = \begin{pmatrix} s_0\frac{\beta_0^2}{a^2} & -s_0\frac{\alpha_0\beta_0}{a^2} & -r_0\frac{\alpha_0\gamma}{a^2} \\ -s_0\frac{\alpha_0\beta_0}{a^2} & s_0\frac{\alpha_0^2}{a^2} & -r_0\frac{\beta_0\gamma}{a^2} \\ 0 & 0 & r_0 \end{pmatrix} \begin{pmatrix} E_{x^+} \\ E_{y^+} \\ E_{z^+} \end{pmatrix} \tag{67}$$

equation which, if relationships (65a), (66a) and (66b) are used, can be expressed as

$$\boxed{\mathbf{E_r} = \begin{pmatrix} -s_0\frac{\beta_0^2}{a^2} & -s_0\frac{\alpha_0\beta_0}{a^2} & -r_0\frac{\alpha_0\gamma}{a^2} \\ s_0\frac{\alpha_0\beta_0}{a^2} & s_0\frac{\alpha_0^2}{a^2} & -r_0\frac{\beta_0\gamma}{a^2} \\ 0 & 0 & r_0 \end{pmatrix} \exp\left(2i\beta_0 y\right)\mathbf{E_i}} \tag{68}$$

which finally provides with the necessary relationship between reflected and incident fields (and thus reflected and incident polarizations) by means of the previously derived r_0 and s_0 Rayleigh coefficients.

Despite the analysis being made for rectangular grooves, it is very common for high power transmission lines to use sinusoidal or other smoothed profile grooves in order to cope with the possibility of arcing. The standard procedure in these cases is to make an initial design with the rectangular grooves and make the smoothed profile directly from it. As this initial design will be taken as a reference, the actual methodology for making the smoothed profile from the rectangular one is of little interest. Then, this smoothed profile should be measured for it to be compared with the canonical theory (i.e. the Rayleigh-modal expansion on rectangular grooves as seen above). For this to be made, measurements should be fitted to results from canonical theory calculations with the effective height (h) and the effective groove width (c) as parameters. Usually, the angular offset is taken as an extra parameter in order to take into account possible positioning inaccuracies. On the other hand, the period (d) is often fixed as the periods from the smoothed and rectangular profiles are built the same. Once the optimization has taken place, the fitted parameters allow for an identification with the smoothed profile parameters (period and amplitude in case of a sinusoidal). Finally, the ratio between the desired canonical parameters (i.e. those needed for the design) and the ones obtained by fitting should also be applied to get the desired smoothed profile from the measured one. This procedure is well described in [11].

In particular this methodology was applied to the QTL1 polarizer mirrors, being the rest (QTL2, 28GHz system) rectangular-grooved ones. Hence, when given across this document, values of QTL1 mirror grooves refer to the rectangular effective parameters.

4.2 Polarization changes induced by waveguide bends

The two continuous curvature bends supplied by General Atomics (GA) and used in the 28 GHz transmission waveguide modify the wave polarization since they introduce a phase difference between the components of the electric field parallel and perpendicular to the curvature plane of the bend (see figure 17).

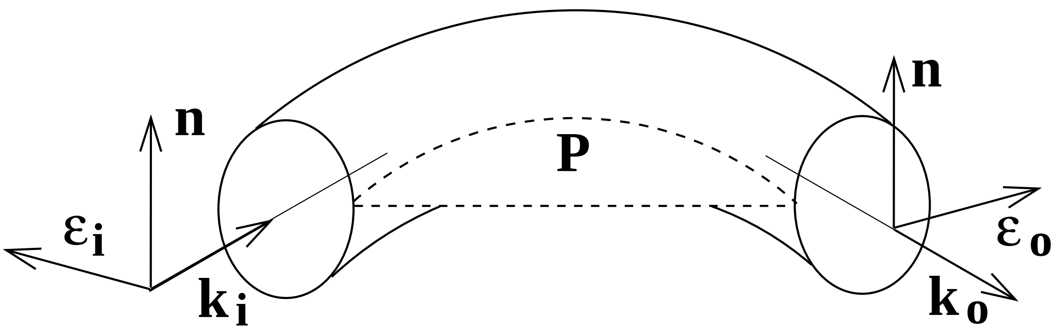

Figure 17: Calculating the wave polarization changes in a bend. The plane **P** is the curvature plane of the bend, similar to the incidence plane of figure 7.

As we have seen in section 3 the complex amplitudes of both incident (i) and output (o) wave electric fields can be written in each local wave reference system ($\boldsymbol{\epsilon}_i, \mathbf{n}, \mathbf{k}_i$ and $\boldsymbol{\epsilon}_o, \mathbf{n}, \mathbf{k}_o$) as

$$
\begin{aligned}
\mathbf{E}^i &= a_1^i \exp(i\delta_1^i)\boldsymbol{\epsilon}_i + a_2^i \exp(i\delta_2^i)\mathbf{n} \\
\mathbf{E}^o &= a_1^o \exp(i\delta_1^o)\boldsymbol{\epsilon}_o + a_2^o \exp(i\delta_2^o)\mathbf{n}
\end{aligned}
$$

The polarization properties of the input and output waves (see section 3, eqs.(11)) are fully determined by $r_i \equiv a_2^i/a_1^i, r_o \equiv a_2^o/a_1^o, \delta_i \equiv \delta_2^i - \delta_1^i$ and $\delta_o \equiv \delta_2^o - \delta_1^o$. The result of computer calculations performed by the manufacturer for each bend is shown in table (3).The 28 GHz launching system design is such that the universal polarizer is installed *before* the waveguide bends and therefore each bend modifies consecutively the wave polarization (ψ_i, χ_i) which is obtained after the reflection in the grooved mirrors surface.

"long" bend	"short" bend
$a_1^o \approx a_1^i$; $a_2^o \approx a_2^i$	$a_1^o \approx a_1^i$; $a_2^o \approx a_2^i$
$\delta_o = \delta_i + 2°$	$\delta_o = \delta_i + 24°$

Table 3: Amplitudes and relative phases of the output and input waves in the two bends.

Using (11), we may write the Stokes parameters of the input and the output waves as

$$
\begin{aligned}
s_1^i &= \frac{1-r_i^2}{1+r_i^2} = \cos 2\chi_i \cos 2\psi_i & s_1^o &= \frac{1-r_i^2}{1+r_i^2} = \cos 2\chi_o \cos 2\psi_o \\
s_2^i &= \frac{2r_i \cos\delta_i}{1+r_i^2} = \cos 2\chi_i \sin 2\psi_i & s_2^o &= \frac{2r_i \cos(\delta_i + \Delta_p)}{1+r_i^2} = \cos 2\chi_o \sin 2\psi_o \\
s_3^i &= \frac{2r_i \sin\delta_i}{1+r_i^2} = \sin 2\chi_i & s_3^o &= \frac{2r_i \sin(\delta_i + \Delta_p)}{1+r_i^2} = \sin 2\chi_o
\end{aligned}
\tag{69}
$$

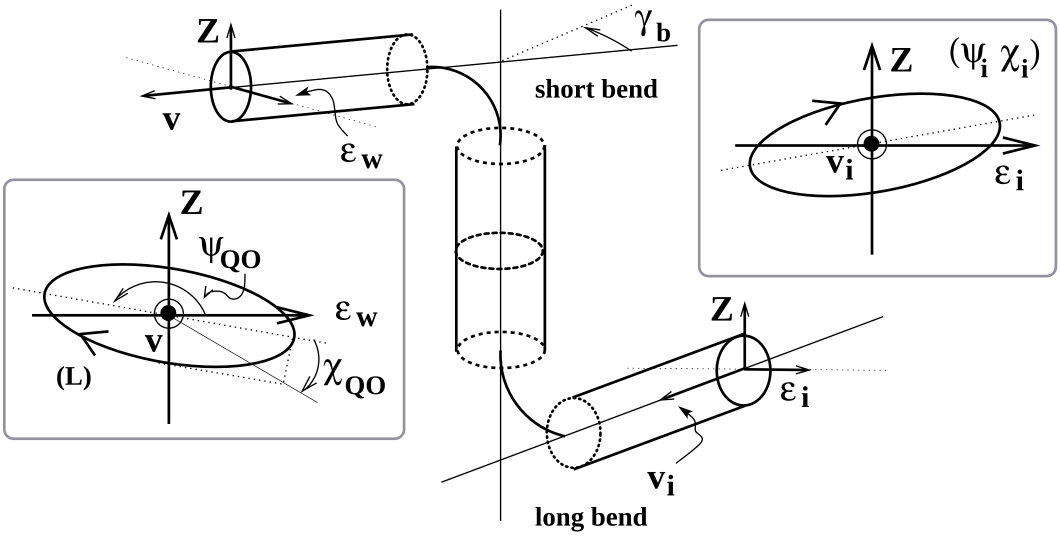

Figure 18: The input wave polarization given by ψ_i and χ_i is modified by the combination of both bends. The final polarization needed to couple a QO–mode is represented in the figure. Figure 4 shows the polarizers setup before the coupling to the waveguide.

where $\Delta_p = \delta_o - \delta_i$ is the phase difference introduced by the bend and we have taken $r_o \approx r_i$. The set of equations (69) allows us to determine the dependencies $\psi_o(\psi_i, \chi_i,)$ and $\chi_o(\psi_i, \chi_i)$. The effect of both bends has to be combined paying attention to the fact that in the present set-up both bends are not coplanar and have curvatures in opposite directions (see figure 18).

4.3 53.2 GHz system

Figure 19 shows the dependence of the azimuth (ψ_1) and the ellipticity angle (χ_1) on the rotation angles α_1 and α_2 of the polarizers installed in the first transmission line (QTL1). The angles ψ_1 and χ_1 are given in the launching reference frame of this line (see figure 9). The two polarizers are positioned at an incidence angle $\Theta_i = 15°$ (see figure 3a). The groove parameters used in the calculation are listed in table (4).

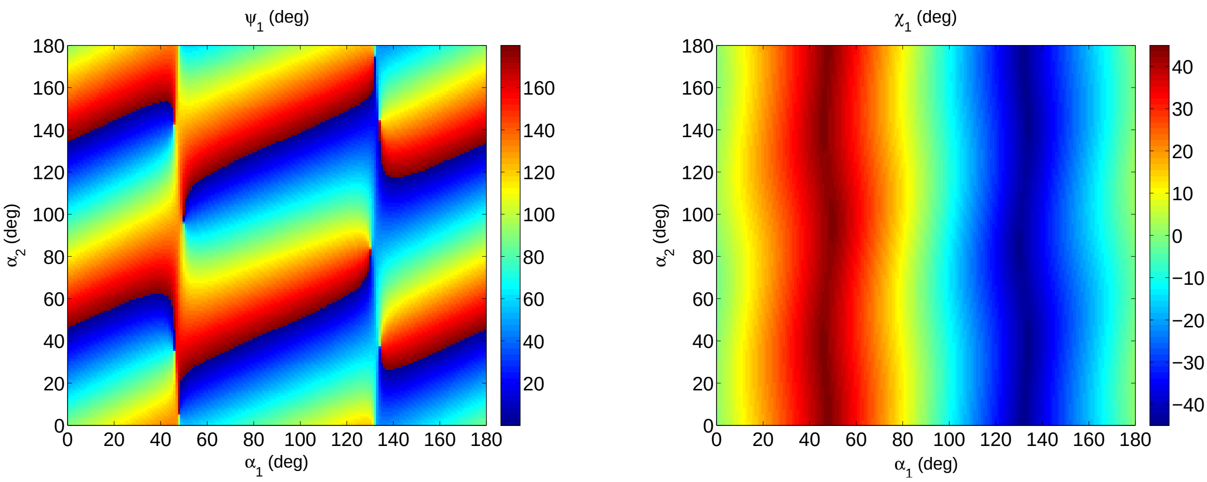

Figure 19: Dependence of ψ_1 and χ_1 on the rotation angles α_1 and α_2 of the QTL1 polarizers.

As we have seen in a previous section, the theoretical polarization angles that are needed to couple a QX–mode with $N_{||} = 0$ on-axis (almost perpendicular propagation in the plasma periphery) are $\psi_{\rm QX} = 58.2°$ and $\chi_{\rm QX} = +1.2°$ (see table 2). To launch a wave with this polarization, a possible pair of polarizer angles would be $\alpha_1 \approx 91°$, $\alpha_2 \approx 106°$.

	QTL1		QTL2
(mm)	$\lambda/8$ polarizer	$\lambda/4$ polarizer	$\lambda/4$ polarizer
h	1.004	1.427	1.427
c	1.691	1.691	1.23
d	3.381	3.381	2.46

Table 4: Parameters of the 53.2 GHz polarizers corrugations.

The second transmission line (QTL2) is only equipped with a polarization rotator (a $\lambda/4$ grooved mirror at an incidence angle $\Theta_i = 45°$, see figure 3b). The dependence of the azimuth (ψ_2) and the ellipticity angle (χ_2) on the rotation angle of this polarizer is represented in figure 20. The theoretical QX–mode in this line ($\psi_{\rm QX} = 58.2°, \chi_{\rm QX} = -1.2°$, see again table 2) can be achieved using $\alpha_2 \approx 22°$. The fraction of QX–mode, $\eta_{\rm QX}$, is also represented in the figure.

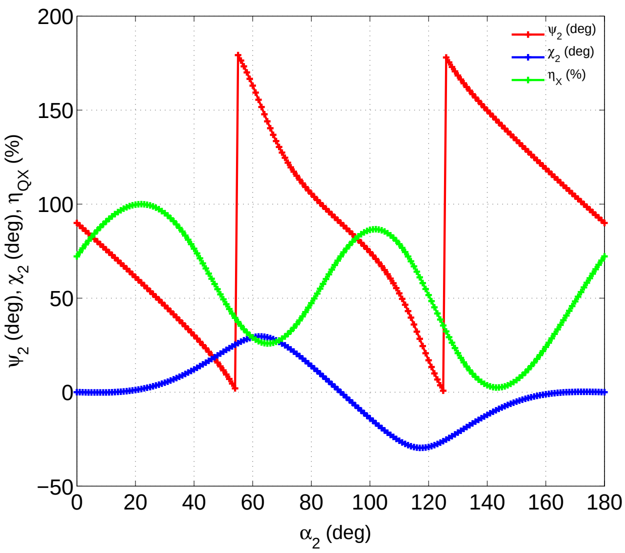

Figure 20: Dependence of ψ_2 (red), χ_2 (blue) and $\eta_{\rm QX}$ (green) on the rotation angle of the QTL2 polarizer.

4.4 28 GHz system

Figure 21 shows the dependence of the azimuth ($\psi_i \equiv \psi_{28}$ before bends) and the ellipticity angle ($\chi_i \equiv \chi_{28}$ before bends) of the polarization ellipse at the waveguide input (see figure 18) on the polarizers rotation angles, α_1 and α_2. The two rectangular groove polarizers are positioned at an incidence angle $\Theta_i = 30°$ (see figure 4). The groove parameters used in the calculation are listed in table (5).

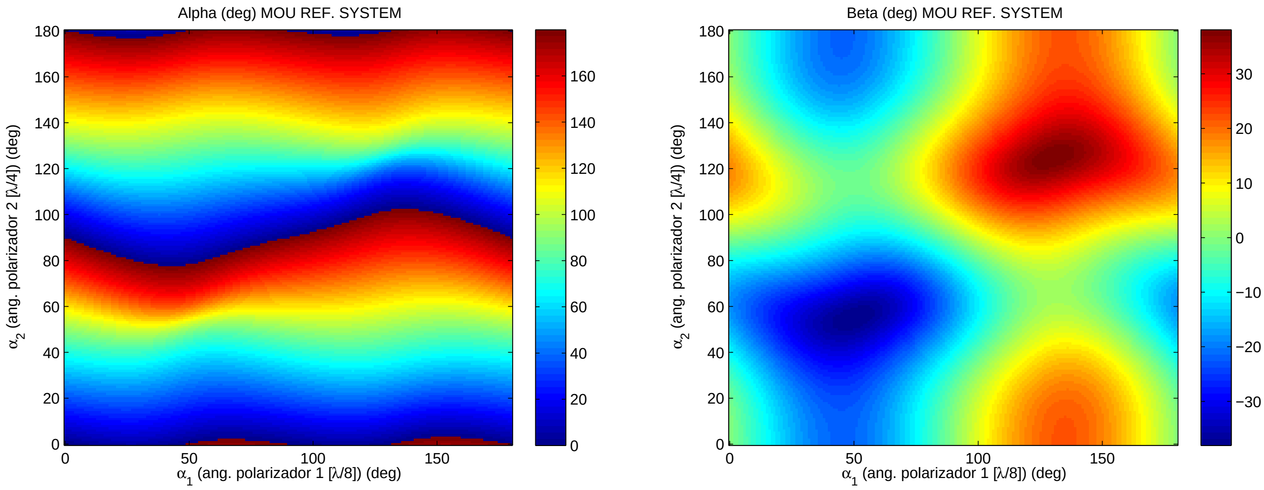

Figure 21: Dependence of ψ_i and χ_i on the rotation angles α_1 and α_2 of the polarizers.

For this incidence angle, there is a strong non linear dependence of ψ_i and χ_i on the position of *both* polarizers. In Appendix C, the dependence of $\psi_i(\alpha_1, \alpha_2)$ and $\chi_i(\alpha_1, \alpha_2)$ on Θ_i is illustrated. Next, we need to know how the waveguide bends modify the values of ψ_i and χ_i. Figure 18 shows the two bends and their relative position. The angle between both curvature planes is $\gamma_b = 25.47°$. As it was stated in 4.2, each bend can be treated separately and then both effects added by taking into account their relative position.

(mm)	First polarizer	Second polarizer
h	1.338	2.676
c	2.500	2.500
d	6.000	6.000

Table 5: Parameters of the 28 GHz polarizers corrugations.

Using (69) iteratively and treating carefully the different coordinates systems we find the results depicted in figure 22, where the final polarization ellipse angles, $\psi_o \equiv \psi_{28}$ after bends and $\chi_o \equiv \chi_{28}$ after bends, are again represented as a function of the polarizers rotation angles. The influence of bends is clearly noticeable in both polarization ellipse angles, in particular the parameter space for achieving an almost circular left handed polarization is enlarged, though a pure circular polarization is no longer available (as the color sidebar in the χ_o case does not reach -45 degrees). In order to achieve the optimum polarization for O mode injection (given by eq. 29) polarizers must be set to $\alpha_1 \approx 51°$ and $\alpha_2 \approx 73°$. Setting the angle of the second polarizer to 0 degrees and rotating only the $\lambda/8$ polarizer we obtain the result represented in figure 23. Moreover, if no grooved mirrors are used, the horizontal polarization ($\psi_i = 0°, \chi_i = 0°$) delivered by the gyrotron is all the same modified. In this case, the polarization angles of the launched radiation and the fraction of power in the desired QO–mode are given by

$$\psi_o \approx +24.2^\circ$$
$$\chi_o \approx -9.2^\circ$$
$$\eta_{\mathrm{QO}} = \frac{1}{2}(1 + \mathbf{s}_{\mathrm{QO}} \cdot \mathbf{s}_{\mathrm{o}}) \approx 0.74$$

where (29) has been used to calculate the stokes vector $\mathbf{s}_{\mathrm{QO}}$.

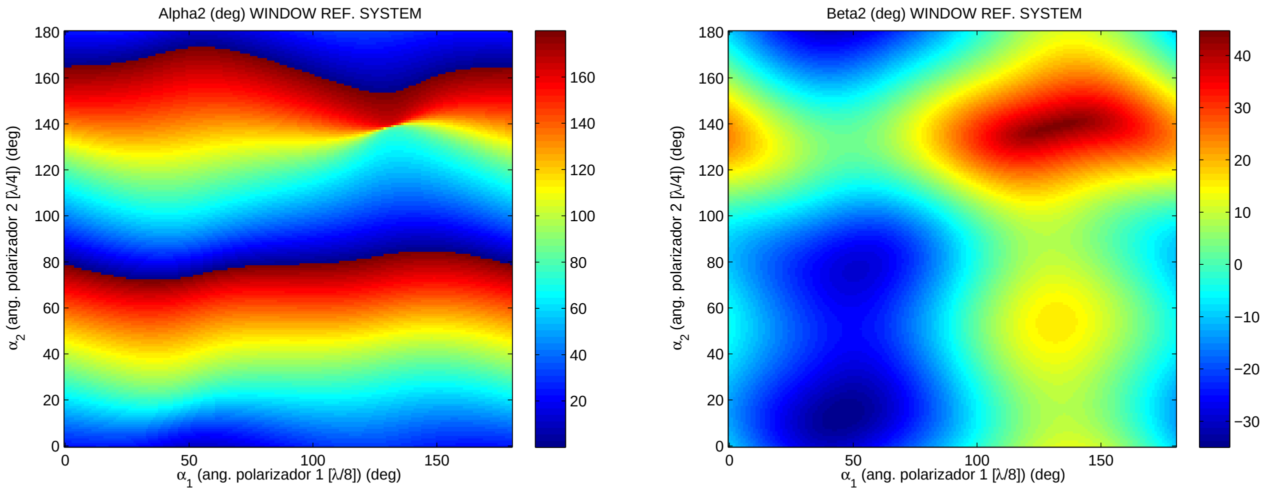

Figure 22: Dependence of the final output polarization angles ψ_o and χ_o on the rotation angles of both polarizers once the effect of the bend has been taken into account.

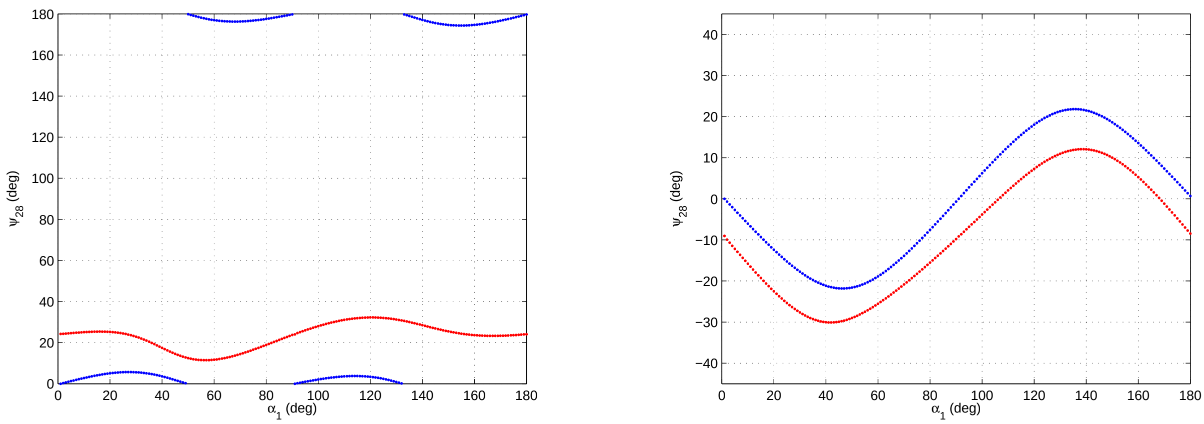

Figure 23: Dependence of ψ_i, χ_i (blue lines) and ψ_o, χ_o (red lines) on the rotation angles of the first polarizer for a constant angle of the second polarizer ($\alpha_2 = 0^\circ$).

Appendices

Appendix A Mirror positioning angles for QTL1 and QTL2

In the 53.2 GHz system, the dependence of the positioning angles a_1 and a_2 of both internal mirrors on the chosen injection location along the magnetic axis is not a straightforward one. Actually, since the intersection between the beam optical axis and the mirror surface is not a fixed point in space (but depends precisely on the mirror angles) and since we are using a non plane mirror surface (beams are refocused by the mirrors), the geometrical calculation of the relation between a_1, a_2, φ and $N_{||}$ is rather complicated [2]. Here we only remind the general behavior represented in figures 24 and 25. It is clear from the figures that, instead of the mirror angles, it is much more convenient to use φ or $N_{||}$ on-axis to characterize the launching direction.

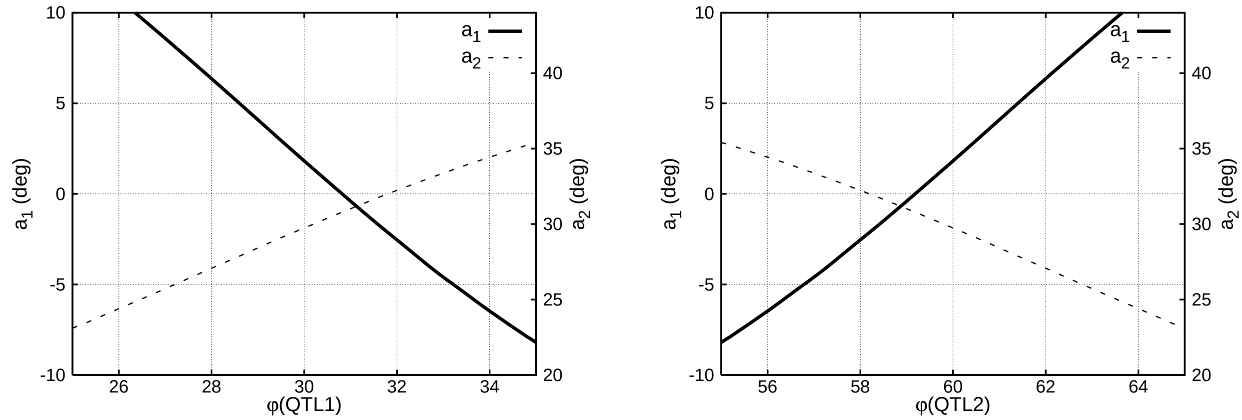

Figure 24: Dependence of the "toroidal" (a_1) and "poloidal" (a_2) mirror positioning angles on the launching direction given by the toroidal TJ–II angle φ for both transmission lines.

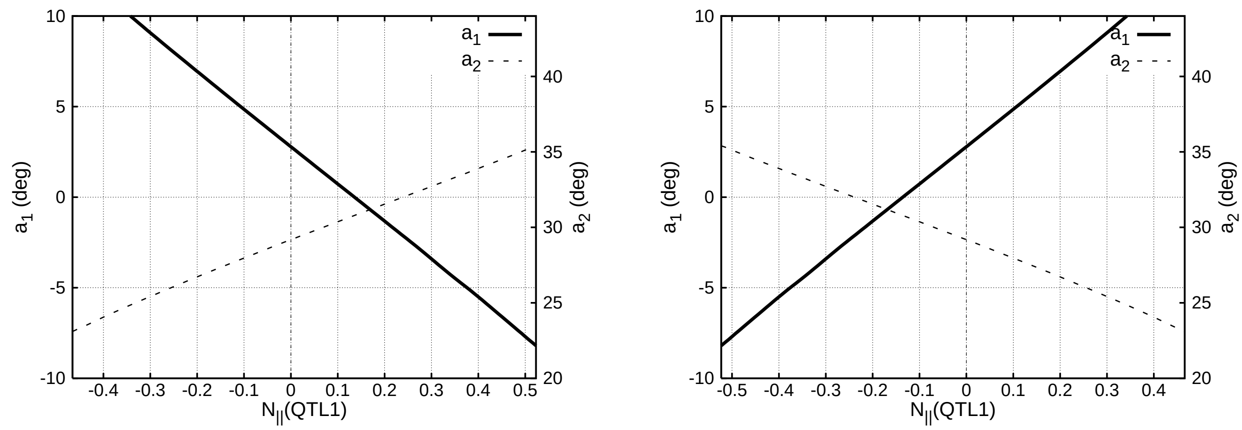

Figure 25: Dependence of the "toroidal" (a_1) and "poloidal" (a_2) mirror positioning angles on the launching direction given by $N_{||}$ on-axis for both transmission lines.

The mirror angles for different values of φ and $N_{||}$ on-axis are presented in tables 6 and 7 of Appendix B. The meaning of a_1 and a_2 and their rotation sense for each launcher is sketched in figure 26. Note that due to the stellarator symmetry both launchers are equally designed, their angles definition is the same and they are positioned one up and another down.

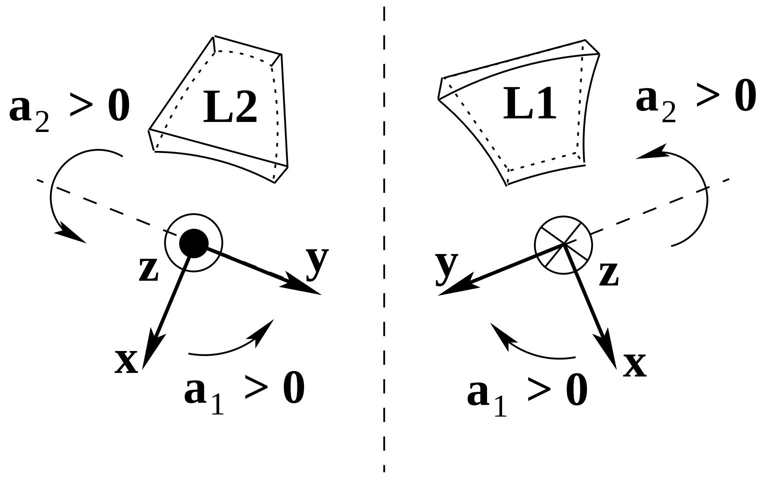

Figure 26: Top view of both launchers showing the rotation sense and the related signs of a_1 and a_2.

Appendix B Polarization angles for QX–mode coupling

Table 6 shows the QTL1 launched wave polarization angles for QX–mode boundary coupling and the rest of parameters, including the mirror positioning angles, that have been discussed in the previous pages. All the angles $a_1, a_2, \theta, \varphi, \psi_{\rm QX}, \chi_{\rm QX}, \psi_{\rm QX}^{axis}, \chi_{\rm QX}^{axis}$ are given in degress. The two last angles with the "*axis*" superscript refers to the polarization angles calculated with the magnetic field on-axis. The difference bewteen these angles and $\psi_{\rm QX}, \chi_{\rm QX}$ is due to the magnetic field shear along the vacuum ray trajectory. At present, these values are not used in the experiments. The data for QTL2 are easily obtained from the ones for QTL1 considering the stellarator symmetry. These are presented in table 7 for completeness.

QTL1										
a_1	a_2	$N_\parallel$	φ	$\lvert B\rvert$	θ	$\psi_{\rm QX}$	$\chi_{\rm QX}$	$\eta_{\rm QX}$	$\psi_{\rm QX}^{axis}$	$\chi_{\rm QX}^{axis}$
12.8	23.1	−0.47	25.0	0.881	113.5	53.5	32.0	0.734	49.3	33.6
12.4	23.3	−0.45	25.2	0.881	112.6	53.7	31.4	0.743	49.3	32.9
12.0	23.6	−0.43	25.4	0.880	111.7	53.9	30.8	0.753	49.3	32.3
11.5	23.9	−0.41	25.6	0.879	110.7	54.0	30.1	0.763	49.4	31.6
11.1	24.1	−0.39	25.8	0.879	109.8	54.2	29.4	0.773	49.4	30.8
10.7	24.4	−0.38	26.0	0.878	108.8	54.4	28.7	0.784	49.5	30.0
10.3	24.7	−0.36	26.2	0.877	107.8	54.6	27.8	0.796	49.5	29.2
9.9	24.9	−0.34	26.4	0.877	106.9	54.8	27.0	0.808	49.6	28.2
9.4	25.2	−0.32	26.6	0.876	105.9	55.0	26.0	0.821	49.7	27.2
9.0	25.5	−0.30	26.8	0.875	104.9	55.2	25.0	0.835	49.8	26.2
8.6	25.7	−0.28	27.0	0.874	103.9	55.4	23.9	0.849	49.8	25.0
8.1	26.0	−0.26	27.2	0.873	102.8	55.6	22.7	0.863	49.9	23.7
7.7	26.3	−0.23	27.4	0.873	101.8	55.8	21.5	0.878	50.0	22.3
7.2	26.5	−0.21	27.6	0.872	100.8	56.1	20.1	0.894	50.1	20.9
6.8	26.8	−0.19	27.8	0.871	99.7	56.3	18.6	0.909	50.3	19.2
6.3	27.1	−0.17	28.0	0.870	98.7	56.5	17.0	0.924	50.4	17.5
5.9	27.4	−0.15	28.2	0.869	97.7	56.7	15.3	0.939	50.5	15.6
5.4	27.6	−0.13	28.4	0.868	96.6	56.9	13.5	0.954	50.6	13.6
5.0	27.9	−0.11	28.6	0.867	95.6	57.2	11.6	0.967	50.7	11.5
4.5	28.2	−0.08	28.8	0.867	94.5	57.4	9.5	0.979	50.8	9.2
4.0	28.4	−0.06	29.0	0.866	93.4	57.6	7.4	0.988	51.0	6.9
3.6	28.7	−0.04	29.2	0.865	92.4	57.9	5.2	0.995	51.1	4.4
3.1	29.0	−0.02	29.4	0.864	91.3	58.1	2.9	0.999	51.2	1.9
2.7	29.3	0.01	29.6	0.863	90.3	58.3	0.6	1.000	51.3	−0.6
2.2	29.5	0.03	29.8	0.863	89.2	58.5	−1.8	0.997	51.5	−3.2
1.8	29.8	0.05	30.0	0.862	88.1	58.7	−4.1	0.992	51.6	−5.7
1.3	30.0	0.07	30.2	0.861	87.1	59.0	−6.3	0.983	51.7	−8.1
0.9	30.3	0.09	30.4	0.860	86.0	59.2	−8.5	0.972	51.9	−10.4
0.4	30.6	0.12	30.6	0.860	85.0	59.4	−10.6	0.958	52.0	−12.6
0.0	30.8	0.14	30.8	0.859	84.0	59.7	−12.6	0.943	52.1	−14.6

QTL1										
a_1	a_2	$N_\parallel$	φ	$\lvert B\rvert$	θ	ψ_{QX}	χ_{QX}	η_{QX}	$\psi_{\mathrm{QX}}^{axis}$	$\chi_{\mathrm{QX}}^{axis}$
−0.5	31.1	0.16	31.0	0.859	82.9	59.9	−14.5	0.927	52.2	−16.6
−0.9	31.3	0.18	31.2	0.858	81.9	60.1	−16.2	0.910	52.4	−18.4
−1.3	31.6	0.20	31.4	0.858	80.9	60.3	−17.9	0.893	52.5	−20.0
−1.8	31.8	0.22	31.6	0.857	79.9	60.5	−19.4	0.875	52.6	−21.5
−2.2	32.0	0.24	31.8	0.857	78.9	60.8	−20.8	0.858	52.7	−22.9
−2.6	32.3	0.26	32.0	0.856	77.9	61.0	−22.1	0.842	52.9	−24.2
−3.0	32.5	0.28	32.2	0.856	76.9	61.2	−23.4	0.826	53.0	−25.4
−3.5	32.7	0.30	32.4	0.856	75.9	61.4	−24.5	0.811	53.1	−26.5
−3.9	33.0	0.32	32.6	0.856	74.9	61.6	−25.5	0.796	53.3	−27.6
−4.3	33.2	0.34	32.8	0.856	74.0	61.8	−26.5	0.782	53.4	−28.5
−4.7	33.4	0.36	33.0	0.855	73.0	62.1	−27.4	0.769	53.5	−29.4
−5.0	33.6	0.38	33.2	0.856	72.1	62.3	−28.2	0.757	53.7	−30.2
−5.4	33.9	0.40	33.4	0.855	71.2	62.5	−29.0	0.745	53.8	−30.9
−5.8	34.1	0.41	33.6	0.856	70.3	62.7	−29.7	0.734	53.9	−31.6
−6.2	34.3	0.43	33.8	0.856	69.4	62.9	−30.4	0.723	54.1	−32.3
−6.6	34.5	0.45	34.0	0.856	68.5	63.1	−31.0	0.714	54.2	−32.9
−6.9	34.7	0.46	34.2	0.856	67.6	63.3	−31.6	0.704	54.4	−33.5
−7.3	34.9	0.48	34.4	0.857	66.8	63.5	−32.1	0.695	54.5	−34.0
−7.6	35.1	0.50	34.6	0.857	65.9	63.7	−32.6	0.687	54.7	−34.5
−8.0	35.3	0.51	34.8	0.857	65.1	63.9	−33.1	0.679	54.8	−35.0

Table 6: Polarization angles for boundary coupling (ψ_{QX}, χ_{QX}) and other relevant parameters, for the QTL1 case. All angles are given in degrees.

QTL2										
a_1	a_2	$N_\parallel$	φ	$\lvert B\rvert$	θ	ψ_{QX}	χ_{QX}	η_{QX}	$\psi_{\mathrm{QX}}^{axis}$	$\chi_{\mathrm{QX}}^{axis}$
12.8	23.1	0.47	65.0	0.881	66.5	53.5	−32.0	0.734	49.3	−33.6
12.4	23.3	0.45	64.8	0.881	67.4	53.7	−31.4	0.743	49.3	−32.9
12.0	23.6	0.43	64.6	0.880	68.3	53.9	−30.8	0.753	49.3	−32.3
11.5	23.9	0.41	64.4	0.879	69.3	54.0	−30.1	0.763	49.4	−31.6
11.1	24.1	0.39	64.2	0.879	70.2	54.2	−29.4	0.773	49.4	−30.8
10.7	24.4	0.38	64.0	0.878	71.2	54.4	−28.7	0.784	49.5	−30.0
10.3	24.7	0.36	63.8	0.877	72.2	54.6	−27.8	0.796	49.5	−29.2
9.9	24.9	0.34	63.6	0.877	73.1	54.8	−27.0	0.808	49.6	−28.2
9.4	25.2	0.32	63.4	0.876	74.1	55.0	−26.0	0.821	49.7	−27.2
9.0	25.5	0.30	63.2	0.875	75.1	55.2	−25.0	0.835	49.8	−26.2
8.6	25.7	0.28	63.0	0.874	76.1	55.4	−23.9	0.849	49.8	−25.0
8.1	26.0	0.26	62.8	0.873	77.2	55.6	−22.7	0.863	49.9	−23.7

QTL2										
a_1	a_2	$N_\parallel$	φ	$\lvert B\rvert$	θ	$\psi_{\rm QX}$	$\chi_{\rm QX}$	$\eta_{\rm QX}$	$\psi^{axis}_{\rm QX}$	$\chi^{axis}_{\rm QX}$
7.7	26.3	0.23	62.6	0.873	78.2	55.8	−21.5	0.878	50.0	−22.3
7.2	26.5	0.21	62.4	0.872	79.2	56.1	−20.1	0.894	50.1	−20.9
6.8	26.8	0.19	62.2	0.871	80.3	56.3	−18.6	0.909	50.3	−19.2
6.3	27.1	0.17	62.0	0.870	81.3	56.5	−17.0	0.924	50.4	−17.5
5.9	27.4	0.15	61.8	0.869	82.3	56.7	−15.3	0.939	50.5	−15.6
5.4	27.6	0.13	61.6	0.868	83.4	56.9	−13.5	0.954	50.6	−13.6
5.0	27.9	0.11	61.4	0.867	84.4	57.2	−11.6	0.967	50.7	−11.5
4.5	28.2	0.08	61.2	0.867	85.5	57.4	−9.5	0.979	50.8	−9.2
4.0	28.4	0.06	61.0	0.866	86.6	57.6	−7.4	0.988	51.0	−6.9
3.6	28.7	0.04	60.8	0.865	87.6	57.9	−5.2	0.995	51.1	−4.4
3.1	29.0	0.02	60.6	0.864	88.7	58.1	−2.9	0.999	51.2	−1.9
2.7	29.3	−0.01	60.4	0.863	89.7	58.3	−0.6	1.000	51.3	0.6
2.2	29.5	−0.03	60.2	0.863	90.8	58.5	1.8	0.997	51.5	3.2
1.8	29.8	−0.05	60.0	0.862	91.9	58.7	4.1	0.992	51.6	5.7
1.3	30.0	−0.07	59.8	0.861	92.9	59.0	6.3	0.983	51.7	8.1
0.9	30.3	−0.09	59.6	0.860	94.0	59.2	8.5	0.972	51.9	10.4
0.4	30.6	−0.12	59.4	0.860	95.0	59.4	10.6	0.958	52.0	12.6
0.0	30.8	−0.14	59.2	0.859	96.0	59.7	12.6	0.943	52.1	14.6
−0.5	31.1	−0.16	59.0	0.859	97.1	59.9	14.5	0.927	52.2	16.6
−0.9	31.3	−0.18	58.8	0.858	98.1	60.1	16.2	0.910	52.4	18.4
−1.3	31.6	−0.20	58.6	0.858	99.1	60.3	17.9	0.893	52.5	20.0
−1.8	31.8	−0.22	58.4	0.857	100.1	60.5	19.4	0.875	52.6	21.5
−2.2	32.0	−0.24	58.2	0.857	101.1	60.8	20.8	0.858	52.7	22.9
−2.6	32.3	−0.26	58.0	0.856	102.1	61.0	22.1	0.842	52.9	24.2
−3.0	32.5	−0.28	57.8	0.856	103.1	61.2	23.4	0.826	53.0	25.4
−3.5	32.7	−0.30	57.6	0.856	104.1	61.4	24.5	0.811	53.1	26.5
−3.9	33.0	−0.32	57.4	0.856	105.1	61.6	25.5	0.796	53.3	27.6
−4.3	33.2	−0.34	57.2	0.856	106.0	61.8	26.5	0.782	53.4	28.5
−4.7	33.4	−0.36	57.0	0.855	107.0	62.1	27.4	0.769	53.5	29.4
−5.0	33.6	−0.38	56.8	0.856	107.9	62.3	28.2	0.757	53.7	30.2
−5.4	33.9	−0.40	56.6	0.855	108.8	62.5	29.0	0.745	53.8	30.9
−5.8	34.1	−0.41	56.4	0.856	109.7	62.7	29.7	0.734	53.9	31.6
−6.2	34.3	−0.43	56.2	0.856	110.6	62.9	30.4	0.723	54.1	32.3
−6.6	34.5	−0.45	56.0	0.856	111.5	63.1	31.0	0.714	54.2	32.9
−6.9	34.7	−0.46	55.8	0.856	112.4	63.3	31.6	0.704	54.4	33.5
−7.3	34.9	−0.48	55.6	0.857	113.2	63.5	32.1	0.695	54.5	34.0
−7.6	35.1	−0.50	55.4	0.857	114.1	63.7	32.6	0.687	54.7	34.5
−8.0	35.3	−0.51	55.2	0.857	114.9	63.9	33.1	0.679	54.8	35.0

Table 7: Polarization angles for boundary coupling ($\psi_{\rm QX}$, $\chi_{\rm QX}$) and other relevant parameters, for the QTL2 case. All the angles are given in degrees.

Appendix C Dependence of polarizers performance on the incidence angle Θ_i

Figures (27), (28) and (29) show the wave polarization dependence on the incidence angle Θ_i for the 28 GHz case. The incidence angle is the same in both grooved mirrors as shown in figure (4). The result for the design value ($\Theta_i = 60°$) was presented in figure (21). Increasing values of Θ_i produce a stronger coupling between the angles α_1 and α_2 of the polarizers. In the ideal case $\Theta_i = 0°$, not achievable in practice, α_2 would only modify the azimuth angle of the polarization ellipse while α_1 would be responsible of changes in both ellipticity and azimuth angles.

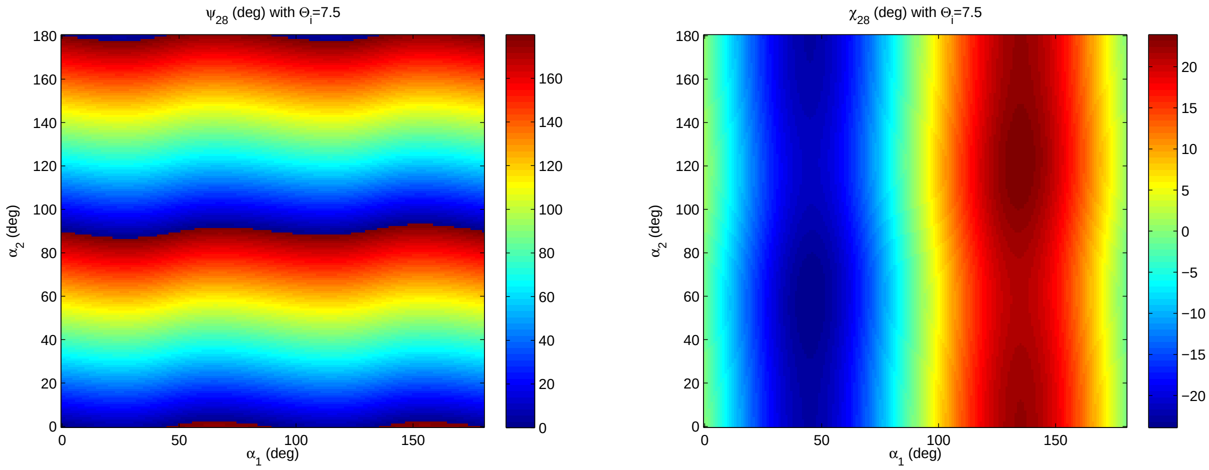

(a) (b)

Figure 27: Dependence of ψ_i (a) and χ_i (b) on the rotation angles α_1 and α_2 of the polarizers for $\Theta_i = 7.5°$.

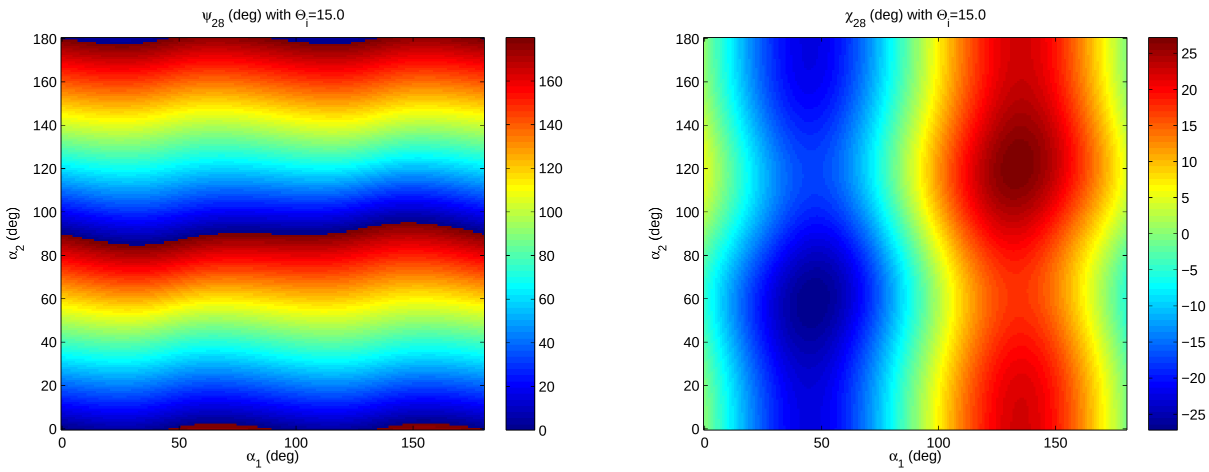

(a) (b)

Figure 28: Dependence of ψ_i (a) and χ_i (b) on the rotation angles α_1 and α_2 of the polarizers for $\Theta_i = 15.0°$.

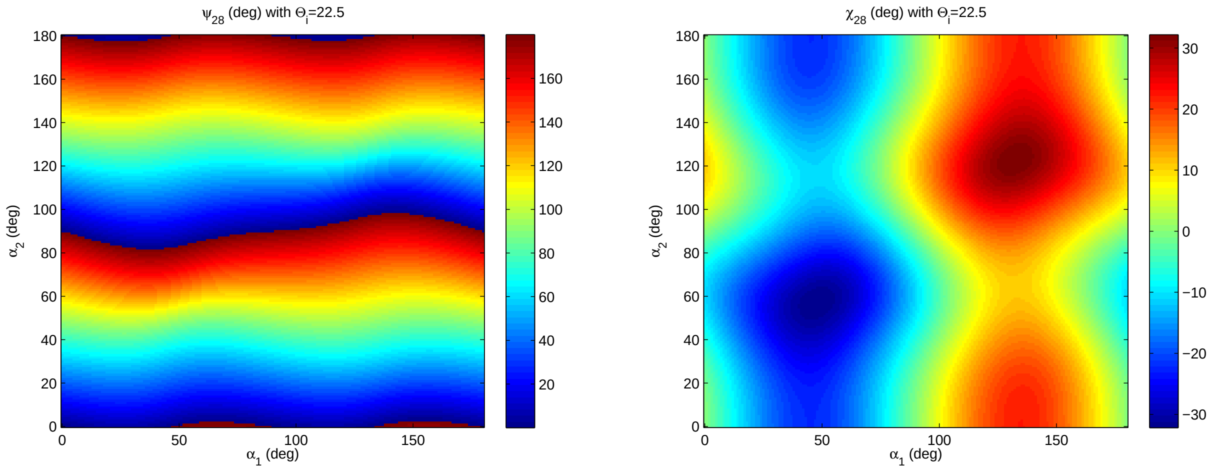

(a) (b)

Figure 29: Dependence of ψ_i (a) and χ_i (b) on the rotation angles α_1 and α_2 of the polarizers for $\Theta_i = 22.5°$.

References

[1] Á. Fernández, W. Kasparek, K. Likin, and R. Martín, "Design of the upgraded TJ-II quasi-optical transmission line," *International Journal of Infrared and Millimeter Waves*, vol. 22, no. 5, pp. 649–660, May 2001. 3

[2] Á. Cappa, V. Tribaldos, K. Likin, Á. Fernández, and R. Martín, *Modification of the heating position using a moveable mirror in the TJ-II ECRH system*, ser. Informes Técnicos Ciemat. Ciemat, Sep 1999, vol. 900. 3, 31

[3] Á. Fernández, K. Sarksyan, N. Matveev, Á. García, M. Medrano, J. Doane, C. Moeller, J. Doncel, A. Pardo, Á. Cappa, F. Castejón, N. Khartchev, M. Tereschenko, A. Tolkachev, and G. Catalán, "Status of the TJ-II electron Bernstein waves heating project," *Fusion Engineering and Design*, vol. 74, no. 1-4, pp. 325–329, Nov 2005. 3

[4] J. Preinhaelter and V. Kopecky, "Penetration of high-frequency waves into a weakly inhomogeneous magnetized plasma at oblique-incidence and their transformation to Bernstein modes," *Journal of Plasma Physics*, vol. 10, no. Aug, pp. 1–12, 1973. 3

[5] J. B. O. Caughman, Á. Fernández, F. Castejón, Á. Cappa, M. C. Carter, D. A. Rasmussen, and J. B. Wilgen, "The electron bernstein wave emission viewing system for the tj-ii stellarator," in *Proceedings of the 14th Joint Workshop on Electron Cyclotron Emission and Electron Cyclotron Resonance Heating*, A. Lazaros, Ed. Heliotopos Conferences Ltd., 2006. 3

[6] M. A. Tereschenko, K. A. Sarksyan, G. M. Batanov, A. S. Sakharov, R. Martín, F. Castejón, Á. Fernández, and Á. Cappa, "Development and use of 3d ray/beam tracing code for plasma heating by ebw in the tj-ii stellarator," in *Proceedings of the 30th EPS Conference on Controlled Fusion and Plasma Physics*, ser. Europhysics conference abstracts, R. Koch and S. Lebedev, Eds., vol. 27A. St. Petersburg: European Physical Society, Jul 2003, pp. 1–18. 4

[7] M. Brambilla, *Kinetic theory of plasma waves: Homogeneous plasmas*, ser. International Series of Monographs on Physics. Clarendon Press, 1998. 6

[8] J. D. Jackson, *Classical Electrodynamics. Third Edition*, 3rd ed. Wiley, Aug. 1998. 9, 10

[9] F. Castejón, Á. Cappa, M. Tereshchenko, and Á. Fernández, "Computation of EBW heating in the TJ-II stellarator," *Nuclear Fusion*, vol. 48, no. 7, Jul 2008. 15

[10] J. M. Garcia-Regaña, Á. Cappa, F. Castejón, J. B. O. Caughman, M. Tereshchenko, A. Ros, D. A. Rasmussen, and J. B. Wilgen, "Electron Bernstein waves emission in the TJ-II stellarator," *Plasma Physics and Controlled Fusion*, vol. 53, no. 6, JUN 2011. 16

[11] D. Wagner and F. Leuterer, "Broadband polarizers for high-power multi-frequency ECRH systems," *International Journal of Infrared and Millimeter Waves*, vol. 26, no. 2, pp. 163–172, Feb 2005. 18, 25

[12] Y. L. Kok and N. C. Gallagher, "Relative phases of electromagnetic-waves diffracted by a perfectly conducting rectangular-grooved grating," *Journal of the Optical Society of America A-Optics Image Science and Vision*, vol. 5, no. 1, pp. 65–73, Jan 1988. 18, 21, 22

[13] R. Petit and L. C. Botten, *Electromagnetic theory of gratings / edited by R. Petit ; with contributions by L. C. Botten ... [et al.].* Springer-Verlag, Berlin ; New York :, 1980. 19

1135- 9420